

**New Large Eddy Simulation Subfilter Turbulence Models Implemented Into the  
Advanced Research WRF Version 3.0**

J. D. Mirocha<sup>1</sup>, J. K. Lundquist<sup>1</sup>, F. K. Chow<sup>2</sup>, B. Kosović<sup>1</sup>

<sup>1</sup>*Lawrence Livermore National Laboratory*

<sup>2</sup>*University of California at Berkeley*

*Corresponding Author Address:*  
Jeffrey D. Mirocha  
Lawrence Livermore National Laboratory  
P. O. Box 808, L-103  
Livermore, California 94551, USA  
email: jmirocha@llnl.gov

LLNL-TR-408080

## 1. Introduction

The Weather Research and Forecasting model (WRF) is a state of the art atmospheric modeling system that can be employed to simulate atmospheric flow over a wide range of scales spanning numerical weather prediction (NWP) to large-eddy simulation (LES) (Skamarock et al. 2005). Historically, WRF has been used primarily to simulate NWP-scale features on computational meshes with horizontal sizes ( $\Delta h$ ) of several kilometers. Increasingly, WRF is being run at scales fine enough to resolve explicitly the important scales of three-dimensional atmospheric turbulence, with horizontal scales less than 100 meters.

Atmospheric turbulence encompasses many different scales which can interact significantly and in nonlinear ways: energy can propagate both up and down scale. Large-scale simulations ( $\Delta h \sim 10s$  of km) use grids that are sufficiently coarse so that no scales associated with atmospheric turbulence are representable on the computational mesh. In such cases, the gridcell average velocity predicted on the nodes comprising the mesh represents the slowly-varying or “mean” state of the flow. Since motions on the scale of atmospheric turbulence cannot be resolved, their influence on the slowly-varying component must be modeled. Typically the horizontal mixing is specified using the deformation of the large-scale flow, while the vertical mixing is prescribed in a so-called planetary boundary layer (PBL) parameterization. Such parameterizations utilize assumptions appropriate for large scales to provide a representation of the gross effects the entire turbulence spectrum on the evolution of the slowly-varying component of the flow field represented by the field variables on the computational mesh (e.g. Stull, 1988). WRF presently contains four representative PBL parameterizations schemes as described in Skamarock et al. (2008).

The LES, in contrast, is a technique in which the turbulence-generating motions within a turbulent flow field are explicitly resolved, while the smaller-scale portion of the turbulence spectrum is removed from the field using a spatial filter. The effects of the filtered scales of motion on the explicitly resolved turbulence field are modeled in a subfilter-scale (SFS) stress model. The SFS model used in a turbulent flow simulation

hence plays a completely different role than that of a PBL parameterization in a large-scale model.

The heuristic reasoning behind the LES approach is that largest turbulent eddies within the flow play a fundamentally different role than smaller eddies. The largest scales are responsible for most of the production of turbulence kinetic energy (TKE) and most of the turbulent transport of both momentum and scalars. These largest scales are highly variable across different types of flows due to strong dependence on forcing conditions such as wind shear, domain geometry, underlying surface characteristics and instabilities. As the turbulence cascades downscale, eddies become smaller, more homogeneous and more isotropic, and function primarily to dissipate energy. These smaller scales of turbulence are hence much more amenable than the largest eddies to a generalized SFS closure model.

The LES technique was developed in the early 1970s and first used to simulate high-Reynolds-number channel flow, then subsequently applied to the atmospheric boundary layer (Deardorff, 1970). Since those early simulations, increases in computational power have permitted expansion of the LES technique to increasingly complicated and computationally intensive flows. Continuing improvement of the technique has resulted in the LES being used to study fundamental aspects of atmospheric turbulence that are difficult or costly to measure in experimental settings (Stevens and Lenschow, 1996; Beare et al., 2004). LES results are routinely used as “data”, and are often employed in the validation as well as the design of atmospheric boundary layer parameterization schemes used in larger-scale models (Cuxart et al., 2006). The validity of such approaches depends crucially on the assumption that the SFS model is providing the correct forcing for the energy producing scales of the turbulence.

Recent advances in high-performance computing coupled with the development of atmospheric models utilizing sophisticated, massively parallel software architecture are extending LES to a wide array of novel uses. The current release of the WRF model, for instance provides an idealized LES capability in the form of two SFS closure models, periodic lateral boundary conditions and the ability to specify surface roughness and heat and moisture fluxes. The addition of a multiple-grid nesting capability greatly expands the potential applications of LES by allowing successively smaller computational meshes

to resolve portions of the domain down to LES scales. Two-way information exchange at the nest interfaces allows both downscale and upscale transfer. This capability promises to usher in a new realm of LES applications involving, for instance, complex terrain and time-dependent mesoscale forcing.

While this convergence of technology provides a framework for potentially powerful analytical and predictive tools, their development and use likewise presents a host of potential problems. Wyngaard (2004) provides an important discussion regarding some fundamental problems associated with modeling the scales of motion between those representable using LES and those for which large-scale PBL parameterization are justified. In a study of two-way nested LES in WRF, Moeng et al. (2007) uncovered a host of technical difficulties involving the communication of information between the nests.

In addition to the important issues raised in Wyngaard (2004) and Moeng et al. (2007), a third component is also required for the successful extension of WRF to the realm of LES, that being the development of adequate models for turbulence-resolving flows. Moeng et al. (2007) modified the existing 1.5-order TKE-based WRF SFS closure model to use diagnostic rather than prognostic TKE to avoid matching subgrid TKE at nest boundaries, and also implemented a two-part eddy viscosity model to correct the predicted eddy viscosity profiles near the surface. However, examination of their simulations reveals persistent and significant errors, including a signature overprediction of near-surface wind shear that is characteristic of the SFS closure approach they used. This result, while beyond the scope of their study, nevertheless illustrates the importance of adequate small-scale models for LES, hence motivating the need for improved SFS turbulence closure in LES models such as WRF.

This paper addresses some of the issues regarding SFS modeling within WRF and presents preliminary results from simulations of idealized flow using the standard WRF SFS models and the new SFS models. Section two discusses the standard WRF model's LES capabilities then introduces the new SFS models. Section three presents a demonstration of the improvements afforded by the new SFS models. A discussion, conclusions and suggestions for future research are presented in Section four.

## 2. Large-eddy simulation using WRF

The standard configuration of the WRF model is limited in its applicability as a large eddy simulation by two factors. Firstly, the current WRF release contains only two simple SFS models, each of which contain several well-known deficiencies. Second, the standard WRF model contains no explicit low-pass filter. Rather, the grid, coupled with the discrete numerics, implicitly provides the filtering that separates the fields into resolved and subfilter components. This approach to filtering is another source of error.

### 2.1 Standard WRF subfilter turbulence closures

Both of the standard WRF subgrid models, the Smagorinsky and the TKE subgrid models, suffer from several fundamental deficiencies. Firstly, the Smagorinsky model uses a constant which, while adjustable, cannot be generalized to work well across different grid resolutions, flow regimes, or even in different regions within the flow (e.g. Ciofalo, 1994). The second closure, which uses a 1.5-order prognostic subgrid TKE, mitigates this problem somewhat by reducing its dependence on model constants. However, constants still appear, both in the formulation of the eddy diffusivity coefficient and in the formulation of the dissipation term in the subgrid TKE equation. Both models assume that turbulence production and dissipation balance locally. This assumption, while implicit in the derivation of the Smagorinsky closure, is explicit in the formulation of the dissipation term in the TKE equation. Assuming local balance between production and dissipation of TKE is of questionable validity in the presence of terrain heterogeneity or instabilities, for instance, or at horizontal resolutions on the order of tens of meters in which advection of TKE is a significant term (Lundquist and Chan, 2007). An additional deficiency of both of these models is failure to include backscatter, which has been shown to be extremely important near solid boundaries and in regions of shear or static stability (Mason and Thompson, 1992). Additionally, each of the SGS models relates the stress linearly to the strain rate through an eddy viscosity coefficient. Such an approach is fundamentally at odds with observations that the stress and strain rate tensors are not aligned. Finally, these approaches are not robust in non-neutral or sheared regions of the

flow because they do not predict anisotropy of the normal subgrid stress components which is required in such complex flows. (Kosović, 1997; Kosović and Curry, 2000).

In addition to the liabilities of the standard WRF subgrid models, the use of the grid and discrete numerics as an implicit filter is likewise problematic for several reasons. Firstly, the purpose of the low-pass filter is to physically remove the scales that are not resolvable on the grid while retaining scales larger than the filter width. However the implicit filtering resulting from time advancement using the discretized governing equations does not cleanly separate the unresolvable from the resolved scales of motion. Rather, a range of resolvable scales are attenuated increasingly approaching the grid cutoff. Such partially-resolved scales introduce errors that impact the larger-scale structures within the flow (Chow et al., 2005; Carati, Winckelmans and Jeanmart, 2001). While higher-order numerical difference operators can mitigate the extent of such errors, the various lower-order solvers comprising time advancement in WRF result in considerable numerical error at scales smaller than approximately  $8\Delta x$ . Scales larger than approximately  $8\Delta x$ , while well-resolved, are still impacted by errors in the partially resolved smaller scales, and the incorrect stresses arising from those.

## 2.2 New subfilter turbulence closures implemented into WRF

New subfilter turbulence models have been implemented into WRF to address each of the above discussed issues and improve WRF's LES performance. A “Nonlinear Backscatter and Anisotropy” (NBA) model (Kosović, 1997) has been implemented to address shortcomings of the standard subgrid models, and an algorithm for computing the “Resolvable Subfilter-scale stresses” (RSFS) (following Chow et al., 2005) has been implemented to address errors introduced by the implicit numerical filtering.

The NBA model is based upon a nonlinear constitutive relation that includes second-order terms which account for backscatter and anisotropy effects. The model diagnoses the subgrid-scale stresses using the resolved-scale deformation and rotation, and can optionally use the subgrid TKE predicted by the standard WRF TKE SGS model. Two constants are required, one that accounts explicitly for backscatter, and another that maintains proper alignment between the stress and rate-of-strain tensors (Kosović, 1997).

The RSFS model computes an additional subfilter-scale (SFS) stress that augments the subgrid-scale (SGS) stress. The RSFS stress is simply added to the SGS stress computed using any SGS model. The RSFS model is so named as it represents stresses arising from the portion of the subfilter stress field that exists between the grid and the numerical filter implied by the discrete numerical solvers which, in WRF, provide the filtering (implicitly) that is required for LES. While the computational mesh cleanly separates the field into a region can be represented on the mesh, and one that cannot (the subgrid portion containing scales that are beyond the Nyquist frequency), the effects of numerical discretization give rise to an additional subfilter region which consists of scales that, while larger than the Nyquist frequency, have been attenuated by the discretization errors arising from the numerical solver. This subregion, while beneath the filter, is, in principle, resolvable on the numerical mesh. The stresses associated with scales of motion that would, if resolved, inhabit this region can be partially reconstructed, up to a limit imposed by the discrete numerical errors, and added to the SGS stresses.

Figure 1 illustrates the resolved and subfilter regions with respect to an idealized turbulence energy spectrum.

The RSFS stresses are computed via application of the explicit filter both to the resolved-scale velocities and to the “reconstructed” RSFS velocities. First the (approximate) inverse of the explicit filter is applied to the velocities to obtain the RSFS velocities (reconstruction). Once the reconstructed RSFS velocities have been obtained, the explicit filter is applied to those in a forward manner to obtain the RSFS stresses. This process can be iterated to yield higher-order estimates of the RSFS stresses.

The use of the explicit filter to further separate the flow and attenuate high-frequency error from the resolved-scale portion of the field improves certain characteristics of the larger-scale features within the flow. Use of the improved resolved-scale turbulence field to compute the additional RSFS stresses has been shown to yield a combined SFS + SGS stress field that approaches subgrid stresses obtained in a-priori tests using DNS (Chow et al., 2005).

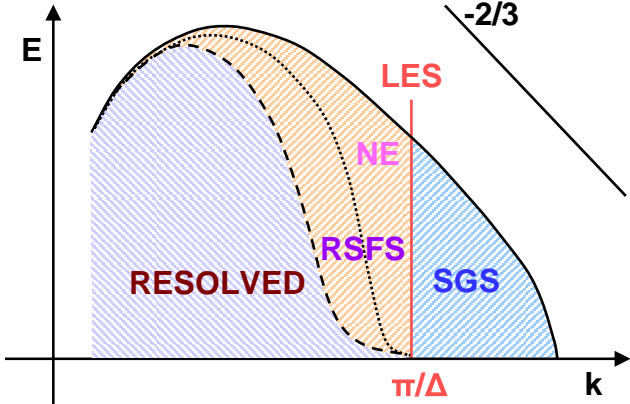


**Figure 1:** Idealized partitioning of spectral energy during LES. The solid line depicts the full energy spectrum for a turbulent flow. The explicit filter (dashed line) improves representation of the resolved component by damping numerical errors due to finite differencing. Velocities in the RSFS region can be reconstructed by filtering, up to a limit imposed by numerical errors (NE, dotted line). The vertical line shows the grid cutoff,  $\pi/\Delta$ . The effect of motions beyond the grid cutoff on the resolved scales is represented with an SGS model. (Figure adapted from Chow et al., 2005).

### 3. Results

#### 3.1 Neutral boundary-layer flow over flat terrain

The new SFS models are compared to WRF's standard SFS models using idealized large-eddy simulations of neutral boundary-layer flow over flat terrain. Each simulation used a constant, uniform geostrophic wind of  $10 \text{ ms}^{-1}$  in the zonal (x) direction, and a logarithmic surface stress using a roughness of 0.1m. The domain was 4096m in each horizontal direction and 1024m in the vertical. Each simulation utilized constant horizontal grid spacing ( $\Delta h$ ) and a staggered vertical grid for which  $\Delta z$  increased by approximately 5% per nodal index above the surface. The upper boundary condition is zero stress, free slip for u and v, and  $w=0$ . The lateral boundaries were periodic.

All of the results presented herein constitute averages in time and space taken from equilibrated simulations. Equilibration was achieved in two steps. An initial 24-hour simulation using the 1.5-order TKE closure was conducted to develop nearly-steady turbulence statistics. Following the initial 24-hour simulation, additional 2-hour simulations were conducted using each SFS model to allow the flow to equilibrate to the

new SFS model physics. After these two initialization steps, simulations were conducted for lengths of time sufficient for the averages to achieve nearly steady values. This length of time ranged from 30 minutes to 9 hours depending on the mesh resolution.

Neutral flow over flat terrain permits comparison to the similarity solution, a logarithmic profile of wind speed (the log law) in the surface layer (roughly the lowest 10% of the boundary-layer height,  $H$ , which, in these simulations is equivalent to the channel depth, the height at which turbulent stresses vanish). Figure 2 shows the profiles of wind speed versus height predicted by the Smagorinsky, TKE, NBA1, and NBA2 SGS closures (with NBA2 using prognostic subgrid TKE) using three mesh resolutions.

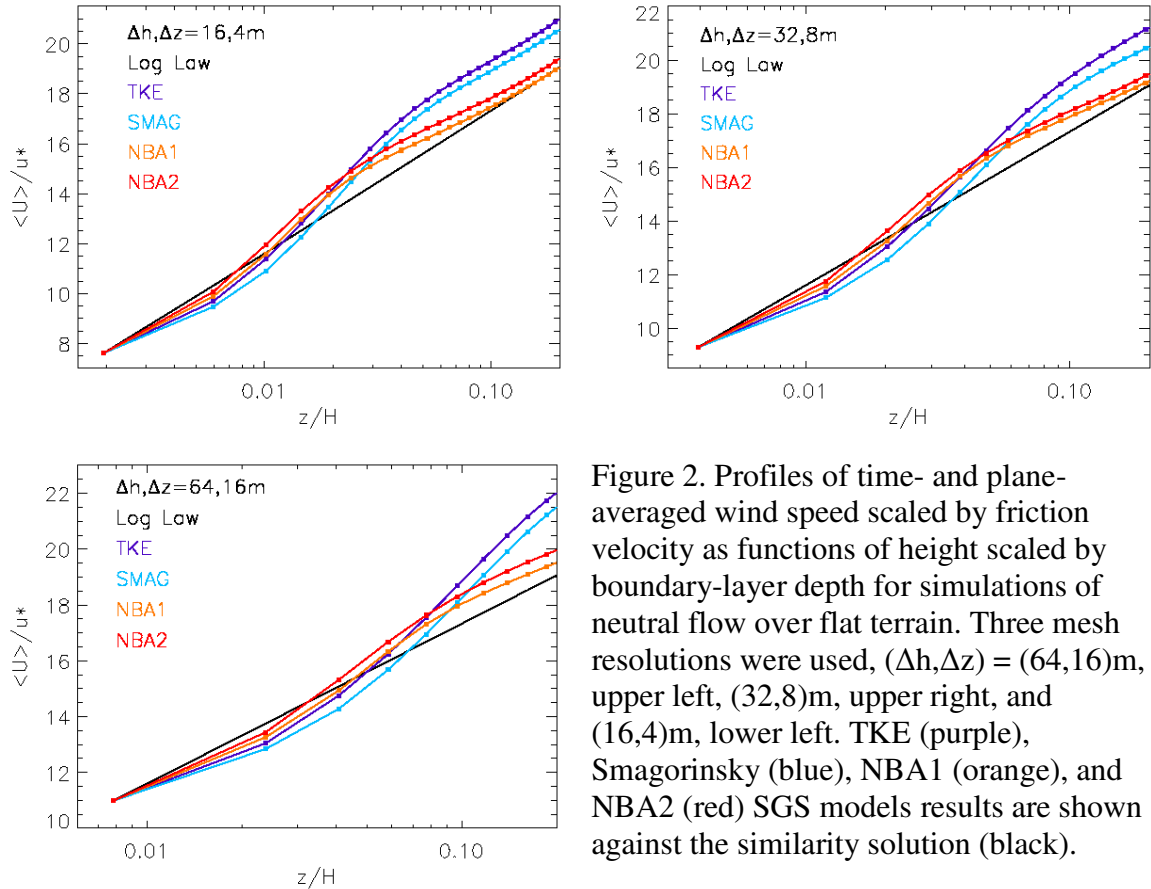


Figure 2. Profiles of time- and plane-averaged wind speed scaled by friction velocity as functions of height scaled by boundary-layer depth for simulations of neutral flow over flat terrain. Three mesh resolutions were used,  $(\Delta h, \Delta z) = (64, 16)$  m, upper left,  $(32, 8)$  m, upper right, and  $(16, 4)$  m, lower left. TKE (purple), Smagorinsky (blue), NBA1 (orange), and NBA2 (red) SGS models results are shown against the similarity solution (black).

In each simulation, the NBA models reduce the errors in the simulated wind speed profile versus the native WRF SGS models. The amount of “overshoot” at the second node above the surface (the first node shown is the first node above the surface) is reduced by each NBA model, with NBA2 predicting the smallest overshoot. Above the

second node, the NBA2 model predicts a slightly larger error than NBA1. Both NBA models significantly improve agreement with similarity solution with increasing  $z/H$ .

Also apparent from Figure 2 is the self-similar shape of the wind speed profile across the different mesh resolutions. Figure 2 also demonstrates that increasing the mesh resolution reduces the magnitude of the error overall for all of the SGS models. The RSFS model results are not included in this figure, as the RSFS stresses do not significantly impact the averaged profiles of mean variables; the impacts of RSFS stresses will be shown below.

Figure 3 depicts time- and plane-averaged spectra of the u-velocity component in the streamwise direction at three heights above the surface for the same mesh configurations as discussed above. Spectra reveal the range of turbulence length-scales resolved during a simulation, and for LES should feature both a low frequency peak and a portion of the inertial subrange (the slope of which is here indicated by the dotted lines). These features indicate that the important eddies are indeed resolved, and that the subgrid parameterization is modeling the effects of eddies well within the inertial subrange.

Figure 3 shows that for each mesh configuration, at each height, the NBA models predict slightly less spectral power at the lowest frequencies, and more spectral power at higher frequencies, indicating energetic contributions from a broader range of eddy sizes. This is particularly noticeable at the coarsest resolution, where the standard WRF SGS models fail to adequately resolve the spectral peak. The differences among the spectra are most pronounced nearer the surface and at coarser resolutions, instances in which the SGS model plays a larger role. Where the flow is well resolved, the spectra are similar.

The role of the RSFS model in modifying the turbulent stresses is shown in Figure 4 which depicts the time- and horizontally-averaged RSFS stresses (dot,dot,dot-dash) in relation to the total (solid), resolved (dot-dash) and SGS (dash) stresses throughout the depth of the boundary layer during a simulation with the NBA2 SGS model with  $(\Delta h, \Delta z) = (32, 8)$ m. The RSFS stresses are shown at two levels of reconstruction, level-zero (the “mixed model”) and level-5. The profiles of the RSFS stresses using the other SGS models are similar (not shown).

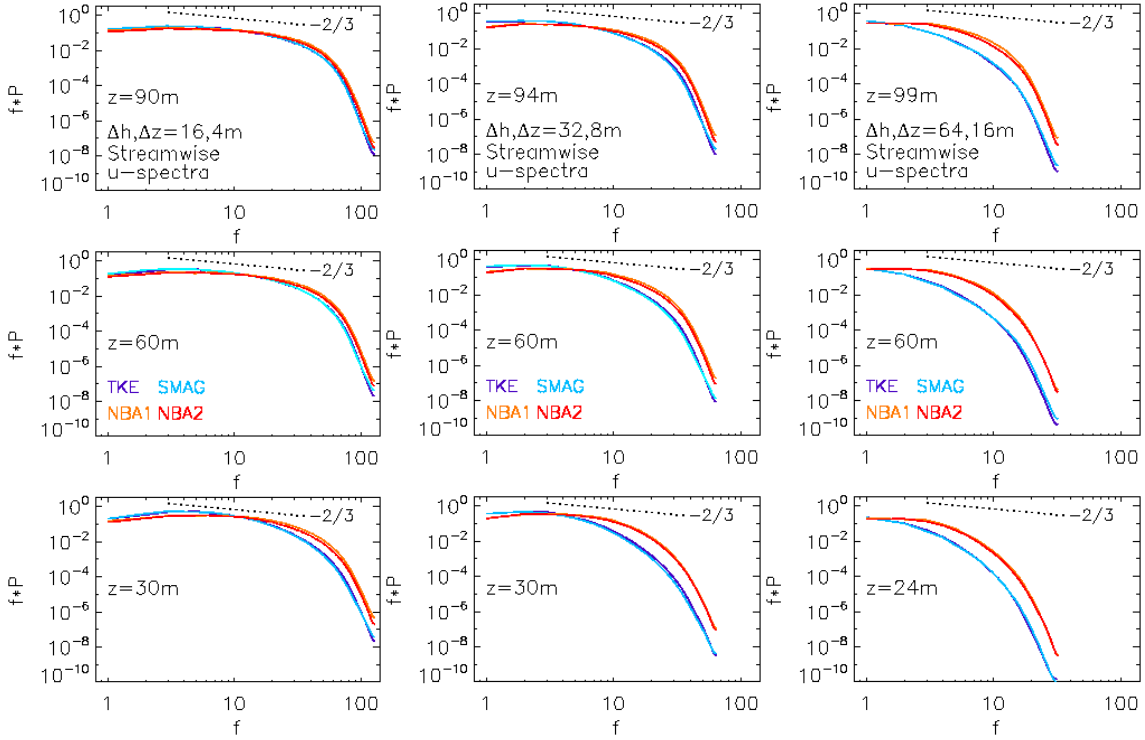


Figure 3. Time- and plane-averaged streamwise  $u$ -velocity spectra at three heights above the surface for simulations of neutral boundary-layer flow over flat terrain using three mesh configurations,  $(\Delta h, \Delta z) = (16, 4)\text{m}$ , left,  $(32, 8)\text{m}$ , middle,  $(64, 16)\text{m}$ , right, and using the TKE (purple), Smagorinsky (blue), NBA1 (orange) and NBA2 (red) SGS models. The expected  $-2/3$  slope in the inertial subrange is shown with the dotted line.

The addition of RSFS stresses decreases the total and SGS stresses only slightly, while reducing the resolved stress significantly, especially in the lower portion of the boundary layer. The reduction in resolved stress is nearly counterbalanced by the RSFS stresses, except near the surface where the RSFS stresses attenuate. Figure 4 indicates that higher orders of reconstruction return only incremental changes in the magnitude of the RSFS stress beyond zeroth order. Given the computational demand of higher orders of reconstruction, this result suggests that zeroth-order reconstruction may be sufficient for many scenarios.

Figure 4 also shows that reconstruction decreases the magnitude of the resolved stress. This reduction in the magnitude of the resolved stress may appear at odds with the goals of LES, however the premium should be on the accuracy of the resolved stresses rather than their magnitude. The largest structures in LES are the most important, as those are the structures that determine the parameters of interest to most applications, including

energy, fluxes and transport. Using the filter to clean up or remove the poorly-resolved smaller scales of the flow and replacing those with a SFS stress that is based on the larger scales that are more accurately resolved provides an improved forcing for those larger scales, hence an improved simulation. Such improvements are difficult to discern from the flat terrain simulations, as the RSFS stresses do not significantly alter the average wind speed distributions or spectra (not shown). However, RSFS stresses do significantly impact the flow over terrain, which is discussed in the following section.

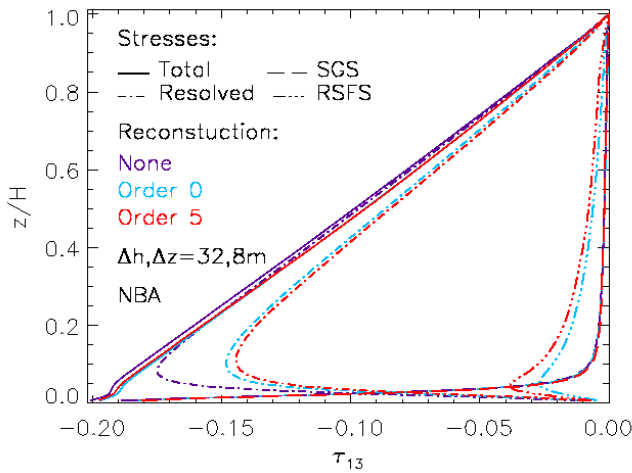


Figure 4. Effects of adding RSFS stresses at level-zero (blue) and level-five (red) reconstruction, versus no RSFS stresses (purple) during simulation of neutral, boundary layer flow over flat terrain using the NBA2 SGS model at a resolution of  $(\Delta h, \Delta z) = (32, 8)$ m.

### 3.2 Neutral boundary-layer flow over an isolated ridge

Simulations of neutral flow over a shallow, Gaussian ridge (symmetric in the y-direction) were conducted to examine the performance of the SFS models over nonuniform terrain. The forcing parameters used for these simulations were identical to those used in the simulation discussed above, however the horizontal dimensions of the domain were reduced from 4096 to 1024m.

Figure 5 shows contours of the zonal ( $u$ ) velocity of the simulated flow using the standard WRF TKE SGS model using a very high-resolution computational mesh of  $(\Delta h, \Delta z) = (8, 2)$ m. Flow is from left to right, and flow separation and reversal in the lee of the hill near the surface is evident. Similar features are simulated by each of the SGS models at this resolution (not shown). Flow reversal such as this has been observed in flume and wind tunnel experiments (Poggi and Katul, 2008; Ayotte and Hughes, 2004).

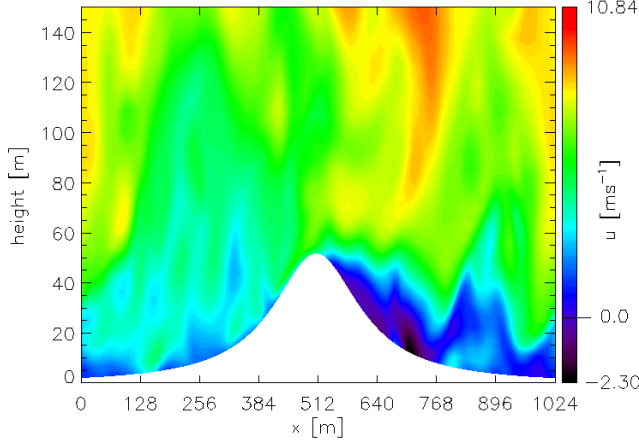


Figure 5. Instantaneous time-height section of zonal velocity from a simulation using  $(\Delta h, \Delta z) = (8, 4)$ m resolution, using standard WRF TKE SGS model. Flow is from left to right, and features separation and reversal in the lee of the hill.

The relative frequencies of zonal velocities during the high-resolution simulations using the TKE (left) and NBA2 (right) SGS models are shown in Figure 6. Distributions at one-minute increments for one hour are shown at four heights above the surface 160m downwind from the hill apex, with the velocities interpolated linearly to the four heights. The NBA2 and TKE models yield very similar distributions, each of reveal separation and flow reversal near the surface. The NBA2 simulation predicts slightly lower velocities aloft, and a relatively larger proportion of negative velocities near the surface.

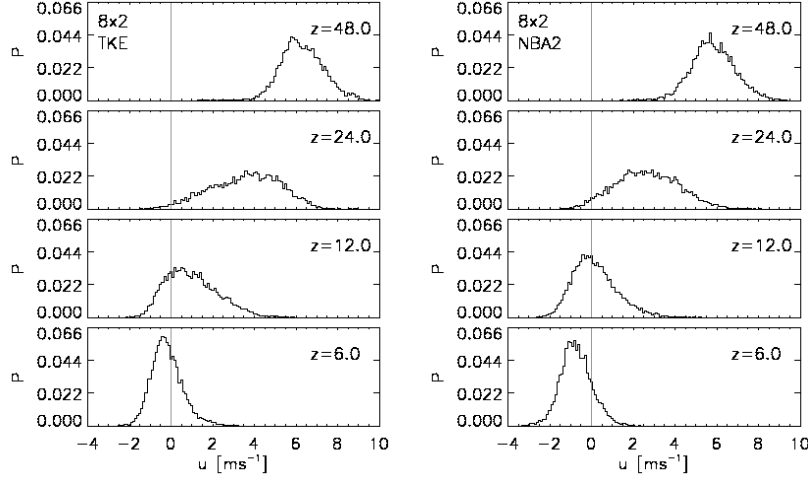


Figure 6. Zonal velocity distributions at four heights above the surface 160m downwind of the hill apex from high-resolution simulations,  $(\Delta h, \Delta z) = (8, 2)$ m, using the TKE (left) and NBA2 SGS models (right).

Figure 7 shows similar distributions from simulations conducted at resolutions coarsened by a factor of two;  $(\Delta h, \Delta z) = (16, 4)$ m. Results from the TKE (left) and NBA2 (right) SGS models are shown. The coarser-resolution simulations reveal a decrease in the proportion of negative velocities approaching the surface relative to the higher-resolution simulations, with larger reductions using the TKE SGS model.

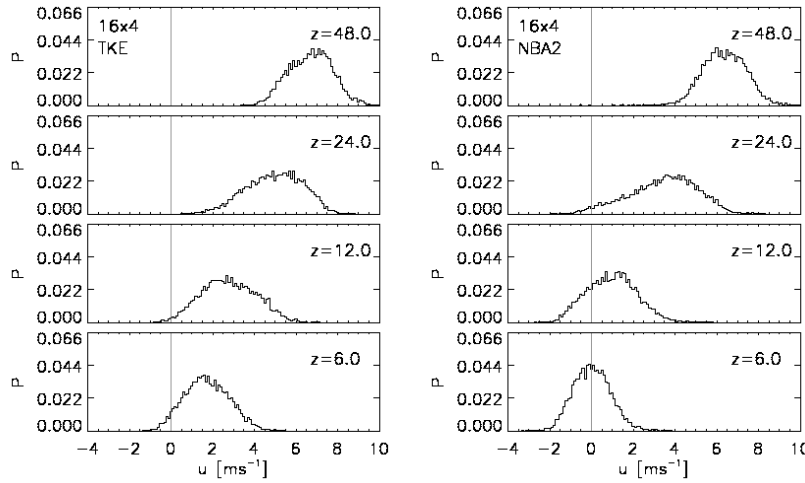


Figure 7. Frequency distributions from  $(\Delta h, \Delta z) = (16, 4)$ m-resolution simulations using TKE (left) and NBA2 (right) SGS models.

Figure 8 shows the distributions from simulations using a computational mesh coarsened by another factor of two,  $(\Delta h, \Delta z) = (32, 8)$ m, using the TKE (left) and NBA2 (right) SGS models. At this yet coarser resolution, flow reversal is all but absent, with the NBA2 SGS model predicting lower velocities near the surface.

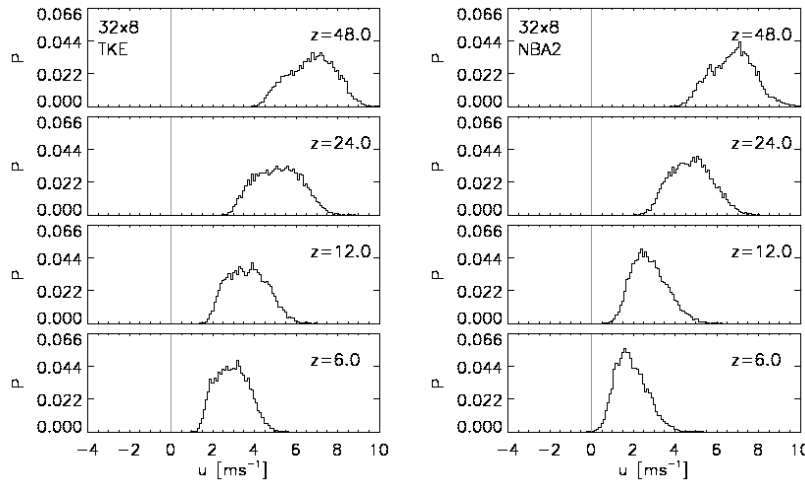


Figure 8. Frequency distributions from  $(\Delta h, \Delta z) = (32, 8)$ m-resolution simulations using TKE (left) and NBA2 (right) SGS models.

Figure 9 shows the effects of adding level-zero RSFS stresses to the coarsest  $(\Delta h, \Delta z) = (32, 8)$ m-resolution simulations using the TKE (left, TKER0) and NBA2 (middle, NBA2R0) SGS models. The effects of higher-order reconstruction (beyond of level-zero) are negligible and are therefore omitted. The RSFS stresses interact with each SGS model differently. When added to the NBA2 SGS model (middle), the RSFS stresses retard the flow near the surface, allowing separation and reversal, with similar distributions near the surface to those of the high-resolution simulations. However, the

NBA2R0 simulation (middle) also excessively retards the flow aloft. The right panel of figure 10 shows that adding a scaled (reducing by fifty percent the RSFS stresses at the second gridpoint above the surface) RSFS stresses to only the first two gridpoints above the surface, rather than at all heights (as in the middle panel) retains flow reversal near the surface, while accelerating the flow aloft. Justifications for using a scaled RSFS stresses include increasing numerical errors approaching the surface, the need separate near-wall models near the surface in high-resolution LES, and potential interactions between RSFS stresses and backscatter from the NBA model near the surface. While the distributions at the two lowest levels using the scaled RSFS stresses are broader than those of the unscaled coarse-resolution (and the highest-resolution) simulations, those above match the distributions from the high-resolution simulation much more closely. These results suggest a potential for combining the NBA2 (and NBA1) SGS models with scaled RSFS stresses to achieve considerable reductions in computational cost.

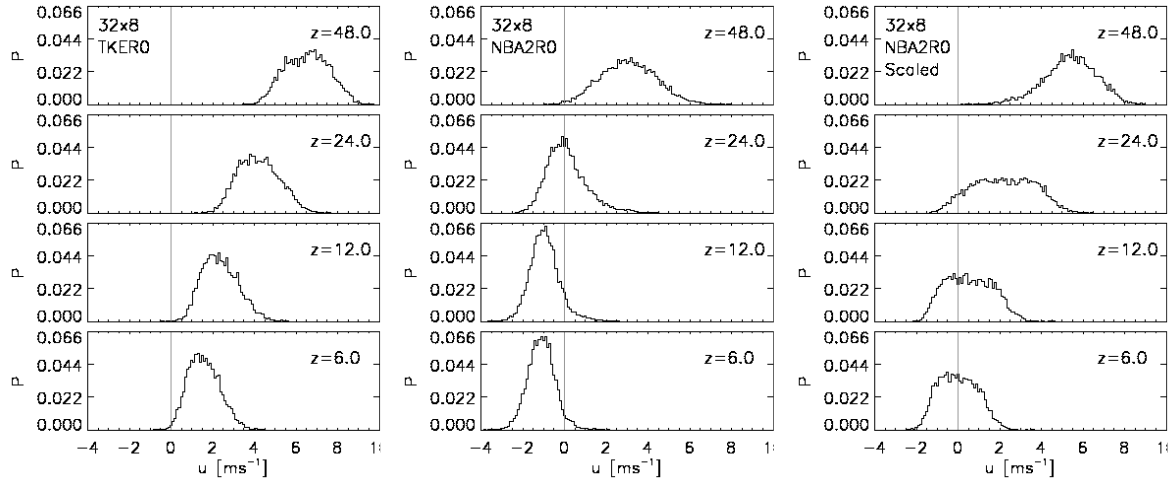


Figure 9. Frequency distributions from  $(\Delta h, \Delta z) = (32, 8)$ m-simulations demonstrating the influences of zeroth-order RSFS stresses added to the TKE (left) and NBA2 (right) SGS models. RSFS stresses added: everywhere (middle); lowest two gridpoints (right).

#### 4.0 Computational Considerations

Figure 10 shows comparisons of distributions from simulations using various resolutions and combinations of SFS models to elucidate potential reductions in computational costs using the new models. The left panel shows distributions from the

$(\Delta h, \Delta z) = (16, 4)$ m-resolution simulation using the NBA2 SGS model (red) and the higher-resolution  $(\Delta h, \Delta z) = (8, 2)$ m simulation using the TKE SGS model (black). The distributions using the NBA2 model at coarser resolution are nearly indistinguishable from those of the higher-resolution simulation using the TKE SGS model. Although the NBA2 model is  $\sim 10\%$  more expensive to run (see Table 1), the computational savings is more than a factor of eight, due to a factor-of-four fewer gridpoints in each horizontal direction and a factor-of-two larger model timestep, not to mention a nearly twenty percent reduction in the number of vertical gridpoints (maintaining the same grid aspect ratio). The middle panel shows a similar comparison between the  $(\Delta h, \Delta z) = (32, 8)$ m-resolution simulation using the NBA2 SGS model (red) and the  $(\Delta h, \Delta z) = (16, 4)$ m-resolution simulation using the TKE SGS model (black). Agreement between the distributions, while impressive, is not as great as in the previous example. The right panel shows a comparison between the coarsest-resolution  $(\Delta h, \Delta z) = (32, 8)$ m simulation using the NBA2 SGS model with the scaled RSFS stresses (red) and the highest-resolutions simulation  $(\Delta h, \Delta z) = (8, 2)$ m using the TKE SGS model (black). Although the distributions differ, the savings represented is nearly two orders of magnitude, considering a factor-of-sixteen reduction of horizontal gridpoints, a factor-of-four reduction in the model timestep, and a thirty eight percent reduction in the number of vertical gridpoints.

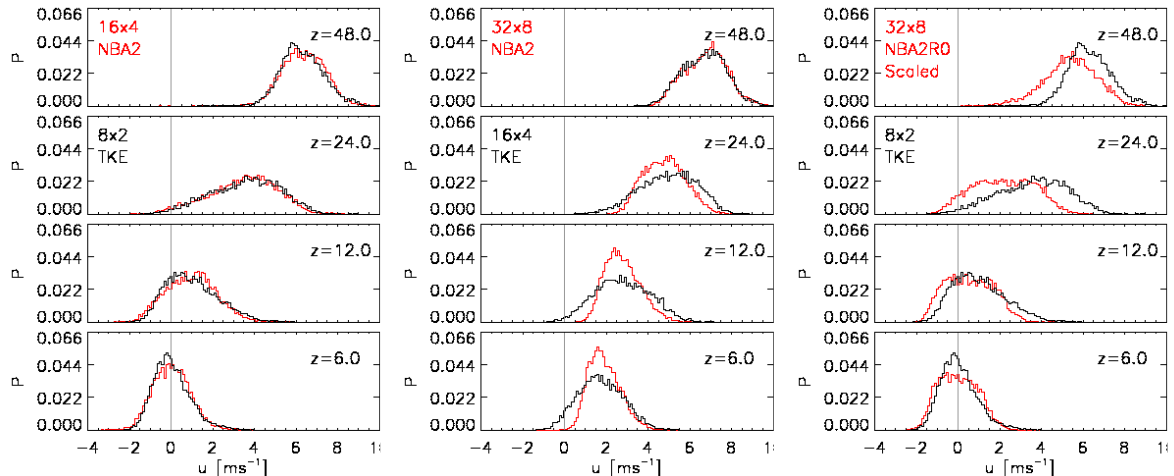


Figure 10. Frequency distributions comparing different resolutions and SFS models: Left;  $(\Delta h, \Delta z) = (16, 4)$ m NBA2 (red) versus  $(\Delta h, \Delta z) = (8, 2)$ m TKE (black); Middle:  $(\Delta h, \Delta z) = (32, 8)$ m NBA2 (red) versus  $(\Delta h, \Delta z) = (16, 4)$ m TKE (black); Bottom:  $(\Delta h, \Delta z) = (32, 8)$ m NBA2 with scaled RSFS (red) versus  $(\Delta h, \Delta z) = (8, 2)$ m TKE (black).

Table 1 contains a brief summary of the relative times required to run each of the subfilter models described in this report.

Table 1: Processor times for simulations using various subfilter stress models. Simulations were conducted using 64 processors (8 processors in each horizontal direction) on a Linux cluster (LLNL’s “Zeus”) of AMD Opteron 2.4 GHz processors. Computational mesh:  $(\Delta h, \Delta z) = (32, 8)m$ ,  $33 \times 33 \times 42 = 45738$  nodes, timestep = 1s.

| SFS model | seconds per iteration<br>using 64 CPUs | minutes required for one-hour<br>simulation using 64 CPUs | % increase |
|-----------|--|---|------------|
| SMAG      | 0.291999                               | 17.5199   | -          |
| TKE       | 0.304220                               | 18.2532   | 4.185      |
| NBA2      | 0.319470                               | 19.1682   | 9.408      |
| NBA2+R0   | 0.342448                               | 20.5469   | 17.277     |
| NBA2+R5   | 0.350279                               | 21.0167   | 19.959     |

#### 4. Conclusions

New subfilter turbulence models have been implemented into the WRF model. Preliminary results suggest that the new SFS models improve the overall behavior of the WRF model in LES applications by reducing some of the errors predicted by the standard WRF SGS models, enhancing the representation of small-scale features, and predicting qualitatively different and correct physical flow phenomena, flow separation behind the hill, at coarser resolution. The new improved subfilter models expand the applicability of the WRF model to new physical contexts via both increased physical realism and by potentially considerable reductions in computational burdens.

Future work will involve continuing validation of the new models in different physical contexts, including complex terrain and non-neutral conditions. A height-dependent formulation for the backscatter coefficient will be explored to potentially reduce errors near the surface in the flat-terrain simulations, and to better interface with the RSFS stresses. Further examination of the height dependence of the RSFS stresses will also be examined.

## Acknowledgements

This work is performed under the auspices of the U.S. Department of Energy by Lawrence Livermore National Laboratory under Contract DE-AC52-07NA27344. LLNL-TR-408080. Staff effort at LLNL and UC Berkeley was supported by the LLNL Laboratory Directed Research and Development (LDRD) program, projects 06-ERD-026 and 09-ERD-038. Computations at LLNL's Livermore Computing were also supported by LDRD. The first author benefited from a WRF Development Testbed Center Visitor appointment.

## References

- Ayotte, K. W., and D. E. Hughes, 2004: Observations of boundary-layer wind-tunnel flow over isolated ridges of varying steepness and roughness, *Bound.-Layer Meteor.*, **112**, 525-556.
- Beare, R. J., M. K. MacVean, A. A. M. Holtslag, J. Cuxart, I. Esau, J-C. Golaz, M. A. Jimenez, M. Khairoutdinov, B. Kosovic, D. Lewellen, T. S. Lund, J. K. Lundquist, A. McCabe, A. F. Moene, Y. Noh, S. Raasch, and P. P. Sullivan, 2004: An intercomparison of large-eddy simulations of the stable boundary layer, *Bound.-Layer Meteor.*, **118**, 247-272.
- Carati, D., G. S. Winckelmans, and H. Jeanmart, 2001: On the modelling of the subgrid-scale and filtered-scale stress tensors in large-eddy simulation. *J. Fluid. Mech.*, **441**, 119-138.
- Chow, F. K., R. L. Street, M. Xue , and J. H. Ferziger, 2005: Explicit filtering and reconstruction turbulence modeling for large-eddy simulation of neutral boundary layer flow, *J. Atmos. Sci.*, **62** , 2058-2077

Ciofalo, M., Large-Eddy Simulation: a Critical Survey of Models and Applications, in *Advances in Heat Transfer*, Vol.25, Chapter 4, pp.321-419, J.P. Hartnett and T.F. Irvine, Jr., eds., Academic Press, 1994.

Cuxart, J., A. A. M. Holtslag, R. J. Beare, E. Bazile, A. Beljaars, A. Cheng, L. Conangla, M. B. Ek, F. Freedman, R. Hamdi, A. Kerstein, H. Kitagawa, G. Lenderink, D. Lewellen, J. Mailhot, T. Mauritzen, V. Perov, G. Schayes, G. J. Steeneveld, G. Svensson, P. Taylor, W. Weng, S. Wunsch, and K-M Xu, 2006: Single-column model intercomparison for a stably stratified atmospheric boundary layer. *Bound.-Layer Meteor.*, **118**, 273-303.

Deardorff, J. W. 1970: Preliminary results from numerical integration of the unstable planetary boundary layer, *J. Atmos. Sci.*, **27**, 1209-1211

Kosović, B., and J. A. Curry, 2000: A large eddy simulation study of a quasi-steady, stably stratified atmospheric boundary layer. *J. Atmos. Sci.*, **57**, 1052-1068

Kosović, B., 1997: Subgrid-scale modelling for the large-eddy simulation of high-Reynolds-number boundary layers. *J. Fluid. Mech.*, **336**, 151-182

Lundquist, J.K. and S. T. Chan, 2007: Consequences of Urban Stability Conditions for Computational Fluid Dynamics Simulations of Urban Dispersion. *J. Appl. Meteorol. Clim.*, **46**, 1080-1097.

Mason, P. J., and D. J. Thompson, 1992: Stochastic backscatter in large-eddy simulations of boundary layers. *J. Fluid. Mech.*, **242**, 51-78

Moeng, C., J. Dudhia, J. Klemp, and P. Sullivan, 2007: Examining the two-way grid nesting for large-eddy simulation of the PBL using the WRF model. *Monthly Weather Review*, **135**, doi: 10.1175/MWR3406.1, 2295-2311.

Poggi, D., and G. G. Katul, 2008: Turbulent intensities and velocity spectra for bare

and forested gentle hills: flume experiments, *Bound.-Layer Meteor.*, **129**, 25-46

Skamarock, W. C., J. B. Klemp, J. Dudhia, D. O. Gill, D. M. Barker, M. G. Duda, X-Y. Huang, W. Wang, and J. G. Powers, 2008: A description of the advanced research WRF version 3, NCAR Technical Note NCAR/TN-475+STR, National Center for Atmospheric Research, 88 pp.

Stevens, B. and D. H. Lenschow, 1996: Observations, experiments and large eddy simulation. *Bull. Amer. Meteor. Soc.*, **82**, 283–294.

Stull, R. B., 1988: *An Introduction to Boundary Layer Meteorology*. Kluwer Academic Publisher, 666 pp.

Wyngaard, J. C., 2004: Toward numerical modeling in the “Terra Incognita”. *J. Atmos. Sci.*, **61**, 1816-1826

## Appendix A: NBA Model Implementation

The NBA model stress tensor can be expressed either as

$$M_{ij} = -(C_s \Delta)^2 \left\{ \begin{array}{l} 2(2S_{mn} S_{mn})^{\frac{1}{2}} S_{ij} \\ + C_1 (S_{ik} S_{kj} - \frac{1}{3} S_{mn} S_{mn} \delta_{ij}) + C_2 (S_{ik} R_{kj} - R_{ik} S_{kj}) \end{array} \right\} \quad (1)$$

Or, alternatively, with  $e_{SGS} \equiv$  subgrid tke, as

$$M_{ij} = -C_e \Delta \left\{ \begin{array}{l} 2(e_{SGS})^{\frac{1}{2}} S_{ij} \\ + \left( \frac{27}{8\pi} \right)^{\frac{1}{3}} C_s^{\frac{2}{3}} \Delta \left[ C_1 (S_{ik} S_{kj} - \frac{1}{3} S_{mn} S_{mn} \delta_{ij}) + C_2 (S_{ik} R_{kj} - R_{ik} S_{kj}) \right] \end{array} \right\} \quad (2)$$

Here,  $S_{ij} = \left( \frac{\partial u_i}{\partial x_j} + \frac{\partial u_j}{\partial x_i} \right)$  is the strain rate tensor,  $R_{ij} = \left( \frac{\partial u_i}{\partial x_j} - \frac{\partial u_j}{\partial x_i} \right)$  is the rotation rate tensor,  $\Delta = (\Delta x \Delta y \Delta z)^{\frac{1}{3}}$ ,  $C_s = \left( \frac{8(1+C_b)}{27\pi^2} \right)^{\frac{1}{2}}$ ,  $C_b = 0.36$ ,  $C_e = \left( \frac{8\pi}{27} \right)^{\frac{1}{3}} C_s^{\frac{4}{3}}$ ,  $C_1 = \frac{960^{\frac{1}{2}} C_b}{7(1+C_b)S}$ ,  $C_2 = C_1$  and  $S = 0.5$ .

Equations 1 and 2 as implemented into WRF are given in component form below. For the implementation that does not use subgrid TKE,  $a = -(C_s \Delta)$  and we have:

$$M_{11} = a \left\{ \begin{array}{l} 2(2D^2)^{\frac{1}{2}} S_{11} + C_1 (S_{11} S_{11} + {}^d \overline{S_{12}} {}^c d \overline{S_{12}} {}^c + {}^e \overline{S_{13}} {}^c e \overline{S_{13}} {}^c - \frac{1}{3} D^2) \\ + C_2 (-2({}^d \overline{S_{12}} {}^c d \overline{R_{12}} {}^c + {}^e \overline{S_{13}} {}^c e \overline{R_{13}} {}^c)) \end{array} \right\}$$

$$M_{22} = a \left\{ \begin{array}{l} 2(2D^2)^{\frac{1}{2}} S_{22} + C_1 (S_{22} S_{22} + {}^d \overline{S_{12}} {}^c d \overline{S_{12}} {}^c + {}^f \overline{S_{23}} {}^c f \overline{S_{23}} {}^c - \frac{1}{3} D^2) \\ + C_2 (2({}^d \overline{S_{12}} {}^c d \overline{R_{12}} {}^c - {}^f \overline{S_{23}} {}^c f \overline{R_{23}} {}^c)) \end{array} \right\}$$

$$M_{33} = a \left\{ \begin{array}{l} 2(2D^2)^{\frac{1}{2}} S_{33} + C_1 (S_{33} S_{33} + {}^e \overline{S_{13}} {}^c e \overline{S_{13}} {}^c + {}^f \overline{S_{23}} {}^c f \overline{S_{23}} {}^c - \frac{1}{3} D^2) \\ + C_2 (2({}^e \overline{S_{13}} {}^c e \overline{R_{13}} {}^c + {}^f \overline{S_{23}} {}^c f \overline{R_{23}} {}^c)) \end{array} \right\}$$

$$M_{12} = a \left\{ \begin{aligned} & 2(2^c D^2)^{1/2} S_{12} + C_1 ({}^c \overline{S}_{11}^d S_{12} + {}^c \overline{S}_{22}^d S_{12} + {}^e \overline{S}_{13}^d f \overline{S}_{23}^d) \\ & + C_2 ({}^c \overline{S}_{11}^d R_{12} - {}^e \overline{S}_{13}^d f \overline{R}_{23} - {}^c \overline{S}_{22}^d R_{12} - {}^f \overline{S}_{23}^d e \overline{R}_{13}^d) \end{aligned} \right\}$$

$$M_{13} = a \left\{ \begin{aligned} & 2(2^c D^2)^{1/2} S_{13} + C_1 ({}^c \overline{S}_{11}^e S_{13} + {}^d \overline{S}_{12}^e f \overline{S}_{23}^e + S_{13} {}^c \overline{S}_{33}^e) \\ & + C_2 ({}^c \overline{S}_{11}^e R_{13} + {}^d \overline{S}_{12}^e f \overline{R}_{23} - {}^f \overline{S}_{23}^e d \overline{R}_{12} - {}^c \overline{S}_{33}^e R_{13}) \end{aligned} \right\}$$

$$M_{23} = a \left\{ \begin{aligned} & 2(2^c D^2)^{1/2} S_{23} + C_1 ({}^d \overline{S}_{12}^f e \overline{S}_{13}^f + {}^c \overline{S}_{22}^f S_{23} + S_{23} {}^c \overline{S}_{33}^f) \\ & + C_2 ({}^d \overline{S}_{12}^f e \overline{R}_{13}^f + {}^c \overline{S}_{22}^f R_{23} + {}^e \overline{S}_{13}^f d \overline{R}_{12} - {}^c \overline{S}_{33}^f R_{23}) \end{aligned} \right\}$$

For the implementation that uses subgrid TKE,  $a = -C_e \Delta$ ,  $b = \left(\frac{27}{8\pi}\right)^{1/3} C_s^{2/3} \Delta$  and we have:

$$M_{11} = a \left\{ \begin{aligned} & 2(e_{sgs})^{1/2} S_{11} + b \left[ \begin{aligned} & C_1 (S_{11} S_{11} + {}^d \overline{S}_{12}^c d \overline{S}_{12}^c + {}^e \overline{S}_{13}^c e \overline{S}_{13}^c - \frac{1}{3} D^2) \\ & + C_2 (-2({}^d \overline{S}_{12}^c d \overline{R}_{12} + {}^e \overline{S}_{13}^c e \overline{R}_{13})) \end{aligned} \right] \end{aligned} \right\}$$

$$M_{22} = a \left\{ \begin{aligned} & 2(e_{sgs})^{1/2} S_{22} + b \left[ \begin{aligned} & C_1 (S_{22} S_{22} + {}^d \overline{S}_{12}^c d \overline{S}_{12}^c + {}^f \overline{S}_{23}^c f \overline{S}_{23}^c - \frac{1}{3} D^2) \\ & + C_2 (2({}^d \overline{S}_{12}^c d \overline{R}_{12} - {}^f \overline{S}_{23}^c f \overline{R}_{23})) \end{aligned} \right] \end{aligned} \right\}$$

$$M_{33} = a \left\{ \begin{aligned} & 2(e_{sgs})^{1/2} S_{33} + b \left[ \begin{aligned} & C_1 (S_{33} S_{33} + {}^e \overline{S}_{13}^c e \overline{S}_{13}^c + {}^f \overline{S}_{23}^c f \overline{S}_{23}^c - \frac{1}{3} D^2) \\ & + C_2 (2({}^e \overline{S}_{13}^c e \overline{R}_{13}^c + {}^f \overline{S}_{23}^c f \overline{R}_{23}^c)) \end{aligned} \right] \end{aligned} \right\}$$

$$M_{12} = a \left\{ \begin{aligned} & 2(e_{sgs})^{1/2} S_{12} + b \left[ \begin{aligned} & C_1 ({}^c \overline{S}_{11}^d S_{12} + {}^c \overline{S}_{22}^d S_{12} + {}^e \overline{S}_{13}^d f \overline{S}_{23}^d) \\ & + C_2 ({}^c \overline{S}_{11}^d R_{12} - {}^e \overline{S}_{13}^d f \overline{R}_{23} - {}^c \overline{S}_{22}^d R_{12} - {}^f \overline{S}_{23}^d e \overline{R}_{13}^d) \end{aligned} \right] \end{aligned} \right\}$$

$$M_{13} = a \left\{ \begin{aligned} & 2(e_{sgs})^{1/2} S_{13} + b \left[ \begin{aligned} & C_1 ({}^c \overline{S}_{11}^e S_{13} + {}^d \overline{S}_{12}^e f \overline{S}_{23}^e + S_{13} {}^c \overline{S}_{33}^e) \\ & + C_2 ({}^c \overline{S}_{11}^e R_{13} + {}^d \overline{S}_{12}^e f \overline{R}_{23} - {}^f \overline{S}_{23}^e d \overline{R}_{12} - {}^c \overline{S}_{33}^e R_{13}) \end{aligned} \right] \end{aligned} \right\}$$

$$M_{23} = a \left\{ 2(e_{sgs})^{1/2} S_{23} + b \left[ C_1 (\overline{S_{12}}^f \overline{S_{13}}^e + \overline{S_{22}}^c \overline{S_{23}} + \overline{S_{23}}^c \overline{S_{33}}^f) + C_2 (\overline{S_{12}}^d \overline{R_{13}}^e + \overline{S_{22}}^c \overline{R_{23}} + \overline{S_{13}}^e \overline{R_{12}}^d - \overline{S_{33}}^c \overline{R_{23}}) \right] \right\}$$

Here  $D^2 = S_{11}S_{11} + S_{22}S_{22} + S_{33}S_{33} + 2(\overline{S_{12}}^c \overline{S_{12}}^d + \overline{S_{13}}^c \overline{S_{13}}^e + \overline{S_{23}}^c \overline{S_{23}}^f)$  and we have

used  $S_{ij} = S_{ji}$ ,  $R_{ij} = -R_{ji}$  and  $R_{ii} = 0$ . The overbars indicate projection from one location within the

Arakawa C-grid to another. For example, in the above expression  $\overline{S_{12}}^c$  indicates projection of deformation element 12, which is defined at ‘d’ points, to ‘c’ points, where  $D^2$  is defined.

In module\_sfs\_nba.F  $D^2$  is calculated and stored in global array smnsmn,  $e_{sgs}$  is grid%tke, the deformations and rotations,  $S_{ij}$  and  $R_{ij}$ , which are in WRF computed as twice the standard definition, are read into local variables ss11, ss12, ..., r12,... and divided by 2. Projected variables are indicated by a suffix letter that designates the point the variable is projected to in the local subroutine. For example, in the computation of stress component m13 in subroutine calc\_m13, ss12e is WRF variable defor12 divided by two and projected to the ‘e’ point. All projections used by the NBA model are illustrated in Appendix C.

## Appendix B. RSFS Model Implementation

The RSFS stress can be most easily apprehended with a brief derivation.

$$\text{LES equations are typically written: } \frac{\partial \bar{u}_i}{\partial x_j} + \frac{\partial (\bar{u}_i \bar{u}_j)}{\partial x_j} = -\frac{\partial \bar{p}}{\partial x_i} - \frac{\partial \tau_{ij}}{\partial x_j} + \dots$$

Here the overbar represents a filter,  $\bar{u}_i = \int G(x-y) u_i(y) dy$

And the subgrid stresses are represented by  $\tau_{ij} \equiv \overline{u_i u_j} - \bar{u}_i \bar{u}_j$

Rather than applying an explicit filter, WRF uses the computational mesh and discrete numerical solvers to provide implicitly the filtering required of LES. If we denote this implicit filtering with a tilde over each variable, and, in addition we apply an explicit filter to WRF, the WRF LES equations can then be written:

$$\frac{\partial \tilde{u}_i}{\partial t} + \frac{\partial (\tilde{u}_i \tilde{u}_j)}{\partial x_j} = -\frac{\partial \tilde{p}}{\partial x_i} - \frac{\partial \tilde{\tau}_{ij}}{\partial x_j} + \dots, \text{ with the subfilter stress given by}$$

$$\tau_{ij} \equiv \overline{u_i u_j} - \bar{\tilde{u}}_i \bar{\tilde{u}}_j.$$

We can expand this stresses by adding and subtracting  $\bar{\tilde{u}}_i \bar{\tilde{u}}_j$  from the subfilter stress:

$$\tau_{ij} \equiv (\overline{u_i u_j} - \bar{\tilde{u}}_i \bar{\tilde{u}}_j) + (\bar{\tilde{u}}_i \bar{\tilde{u}}_j - \bar{\tilde{u}}_i \bar{\tilde{u}}_j) \quad (3)$$

Note that the first term on the right hand side of (3) vanishes in the limit that the discretization errors vanish irrespective of the explicit filter being applied. Hence this term can be associated with the subgrid portion of the subfilter stress—the portion that is beyond the Nyquist frequency and must me modeled irrespective of the accuracy of the numerics. The second term on the right hand side of (3) vanishes in the limit that the filter  $G \rightarrow 1$  irrespective of any discretization errors. Hence this term is associated with the filter, specifically the portion between the grid and the explicit filter, and constitutes the basis of the RSFS stress.

The first term on the right hand side of (3) is thus computed using a standard LES subgrid stress model.

The second term on the right hand side of (3), the RSFS stress, can be computed by applying an explicit filter to the “unfiltered” variables  $\tilde{u}_i$  and  $\tilde{u}_i \tilde{u}_j$ . The “unfiltering” of  $\tilde{u}_i$  is approximated by applying the inverse of the explicit filter,  $G$ , to the prognostic WRF-LES velocity,  $\bar{\tilde{u}}_i$ . Approximate inversion of  $G$  is accomplished numerically using an iterative approach given by:

$$\tilde{u}^*(x) = \bar{\tilde{u}}(x) + (I - G)\bar{\tilde{u}}(x) + (I - G)((I - G)\bar{\tilde{u}}(x)) + \dots \quad (4)$$

Here  $\tilde{u}^*$  represents an approximation of  $\tilde{u}$  up to the level of truncation of the series. Once  $\tilde{u}^*$  is obtained, the RSFS stress is computed just as it appears on the right hand side of (3) with  $\tilde{u}^*$  replacing  $\tilde{u}$  as:

$$\tau_{ij} \equiv \overline{\tilde{u}_i^* \tilde{u}_j^*} - \overline{\tilde{u}_i^*} \overline{\tilde{u}_j^*} \quad (5)$$

Here the overbars indicate application of the explicit filter.

The simplest “zeroth-order” reconstruction uses only the first term on the right hand side of (3);  $\tilde{u}^*$  is given simply by the value of the prognostic velocity at the current time level. Higher-order expressions for  $\tilde{u}^*$  may be obtained by computing additional terms on the right hand side of (3), with the level of reconstruction given by the n-1 term computed. The explicit filter used in (3) and (4) is a three-dimensional, three-point tophat filter.

Algorithmically, the computation of the RSFS proceeds as follows. First the RSFS velocities urec, vrec, and wrec, are obtained from the prognostic WRF velocities u, v and w, respectively. Reconstruction beyond level-zero requires application of the explicit three-dimensional tophat filter, which requires the updating of all HALO and PERIOD communication prior to each application of the filter up to the desired level of reconstruction. The three-dimensional filter requires HALO values at the top and bottom of the domain; the top boundary conditions are free-slip for the horizontal velocities

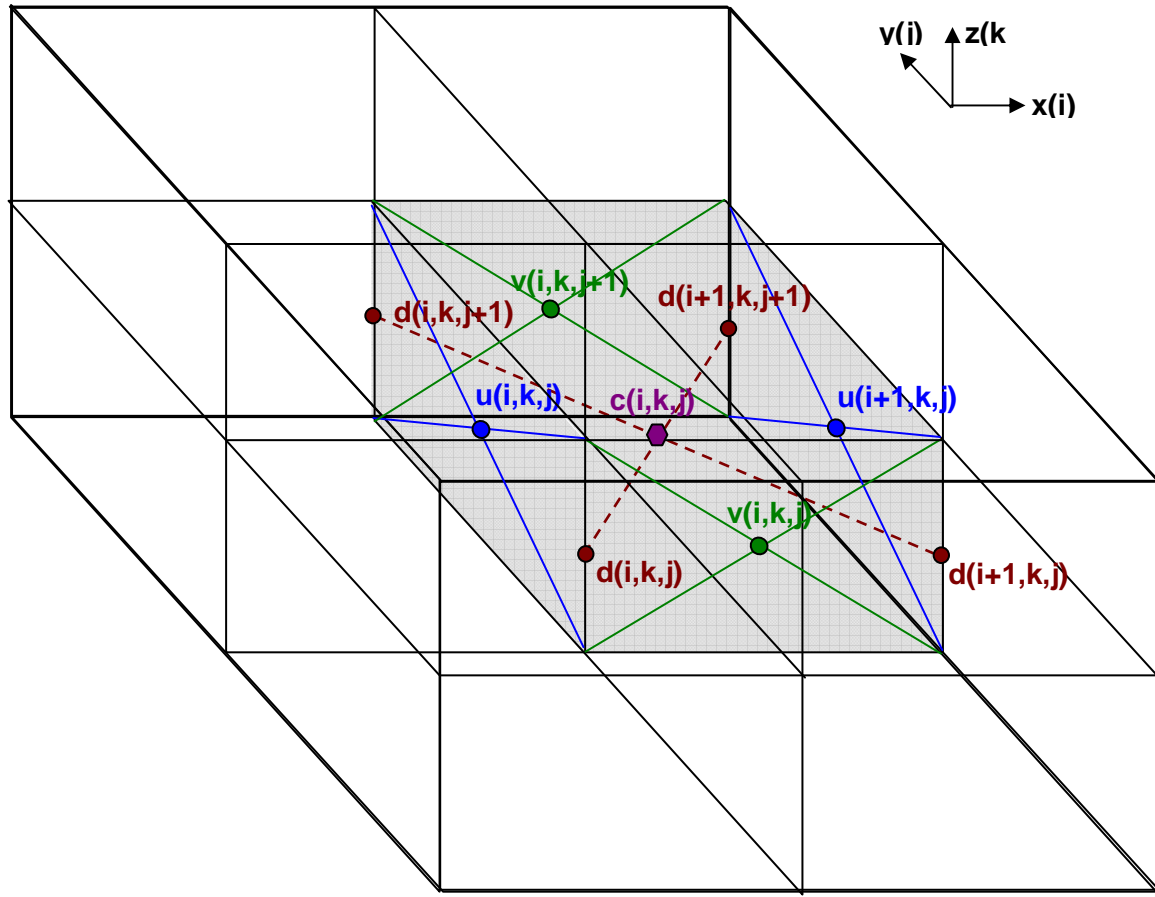
$u, v(ktop + 1/2) = u, v(ktop - 1/2)$  and  $w(ktop) = 0$ . The surface boundary conditions utilize the WRF extrapolation functions to extend u and v to the surface from which w is obtained kinematically.

Once urec, vrec and wrec are obtained they are projected to the locations within the grid at which the stresses are computed and stored in variables whose names the last letter of reflects the projected locations. For example, urec projected to ‘d’ is denoted urecd. Products are also computed in the projection subroutines, for example uvrecd is the product of urecd and vrecd, where urecd and vrecd are urec and vrec, respectively, projected to ‘d’. All projections used by the RSFS model are illustrated in Appendix D.

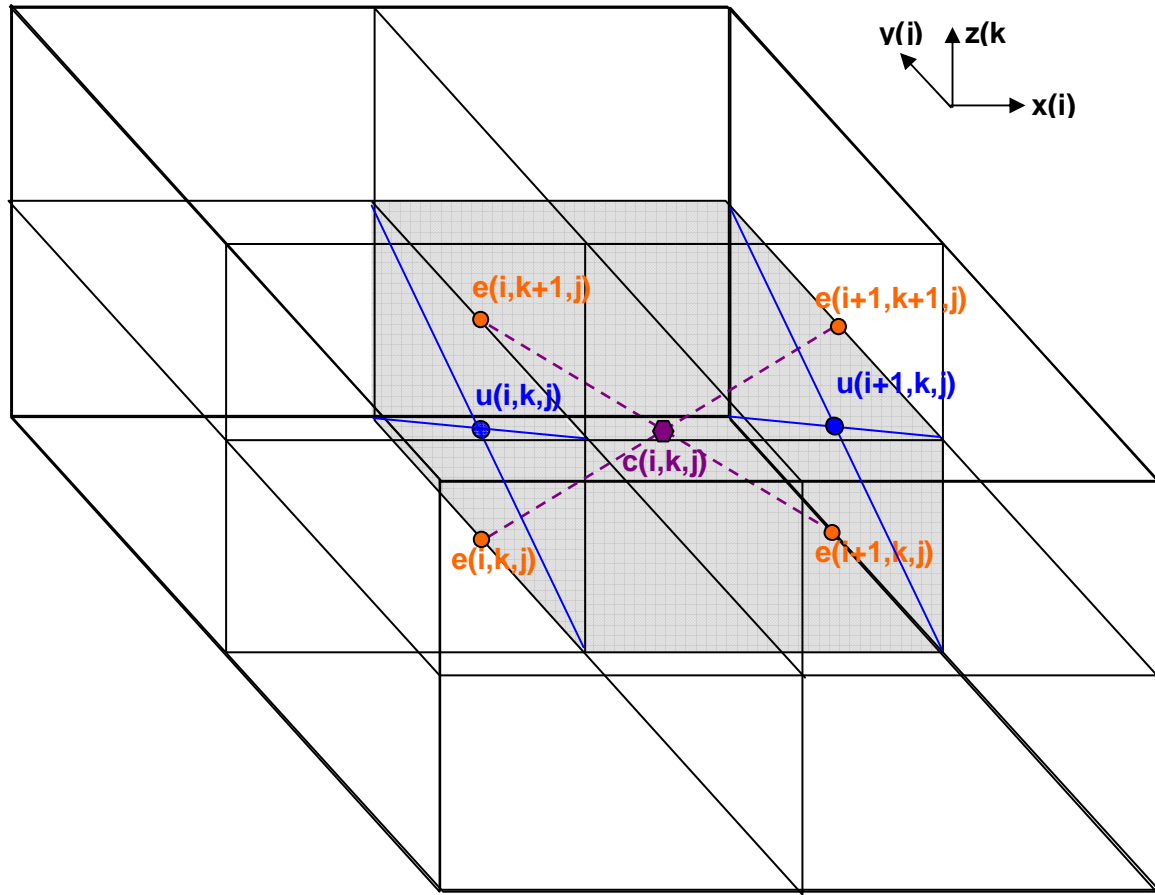
The stresses are finally computed by applying the explicit tophat filter to the projected RSFS velocities with boundary conditions obtained as above. With  $\langle \rangle$  denoting explicit filtering, we obtain the RSFS stresses as:

```
rtau11 = <urecc*urecc> - <urecc>*<urecc>
rtau22 = <vrecc*vrec> - <vrecc>*<vrecc>
rtau33 = <wrecc*wrec> - <wrecc>*<wrecc>
rtau12 = <urecd*vrecd> - <urecd>*<vrecd>
rtau13 = <urece*wrece> - <urece>*<wrece>
rtau23 = <vrecf*wrecf> - <vrecf>*<wrecf>
```

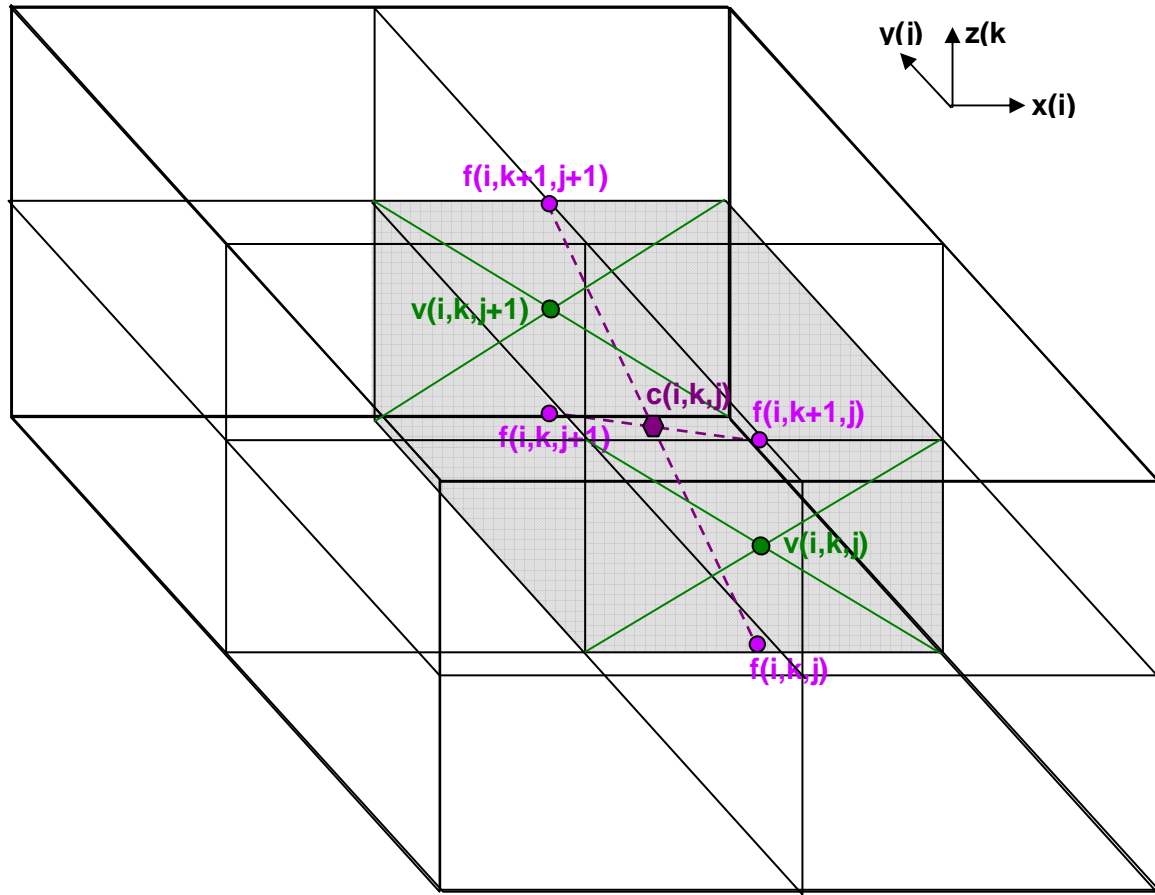
$${}^d \overline{d(i,k,j)}^c = 0.25 * (d(i,k,j+1) + d(i,k,j) + d(i+1,k,j) + d(i+1,k,j+1))$$



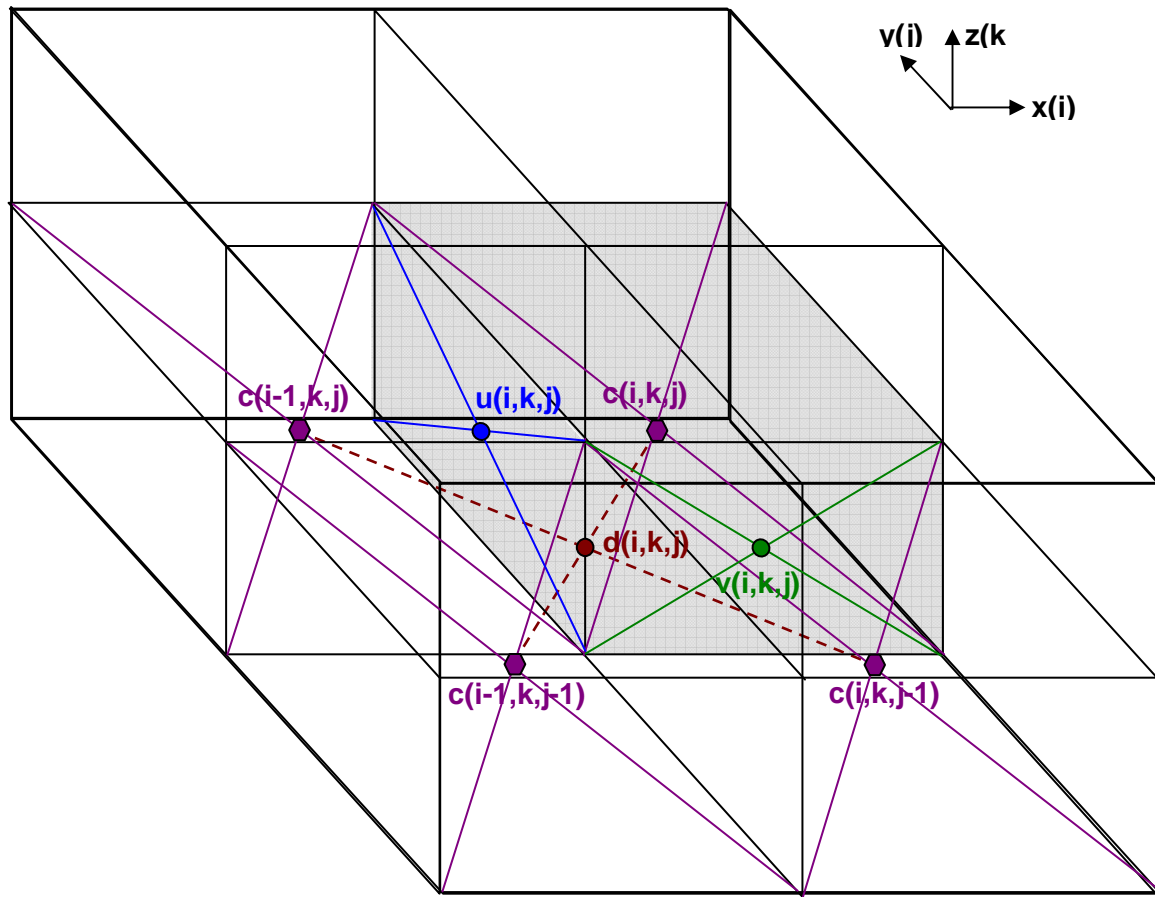
$${}^e \overline{e(i,k,j)}^c = 0.25 * (e(i,k,j) + e(i+1,k,j) + e(i+1,k+1,j) + e(i,k+1,j))$$



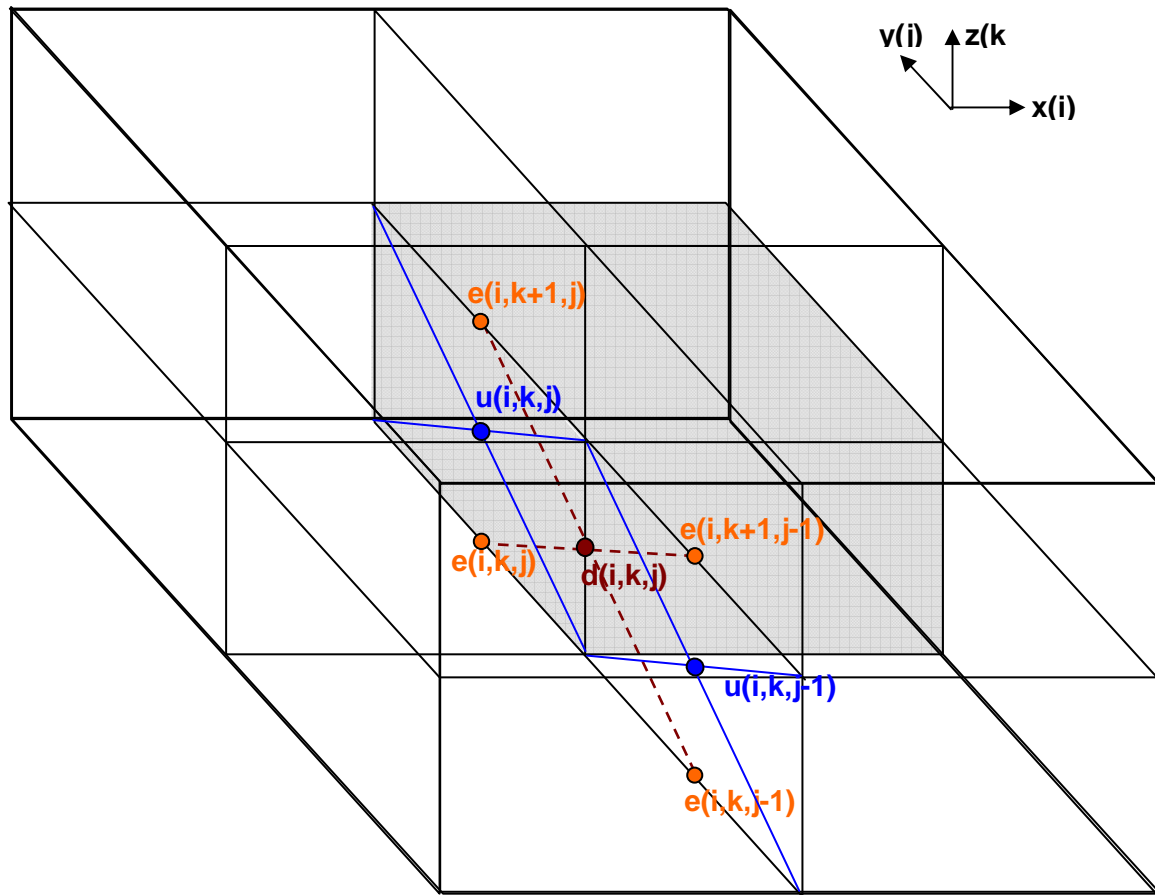
$$f \overline{f(i,k,j)}^c = 0.25 * (f(i,k,j+1) + f(i,k,j) + f(i,k+1,j) + f(i,k+1,j+1))$$



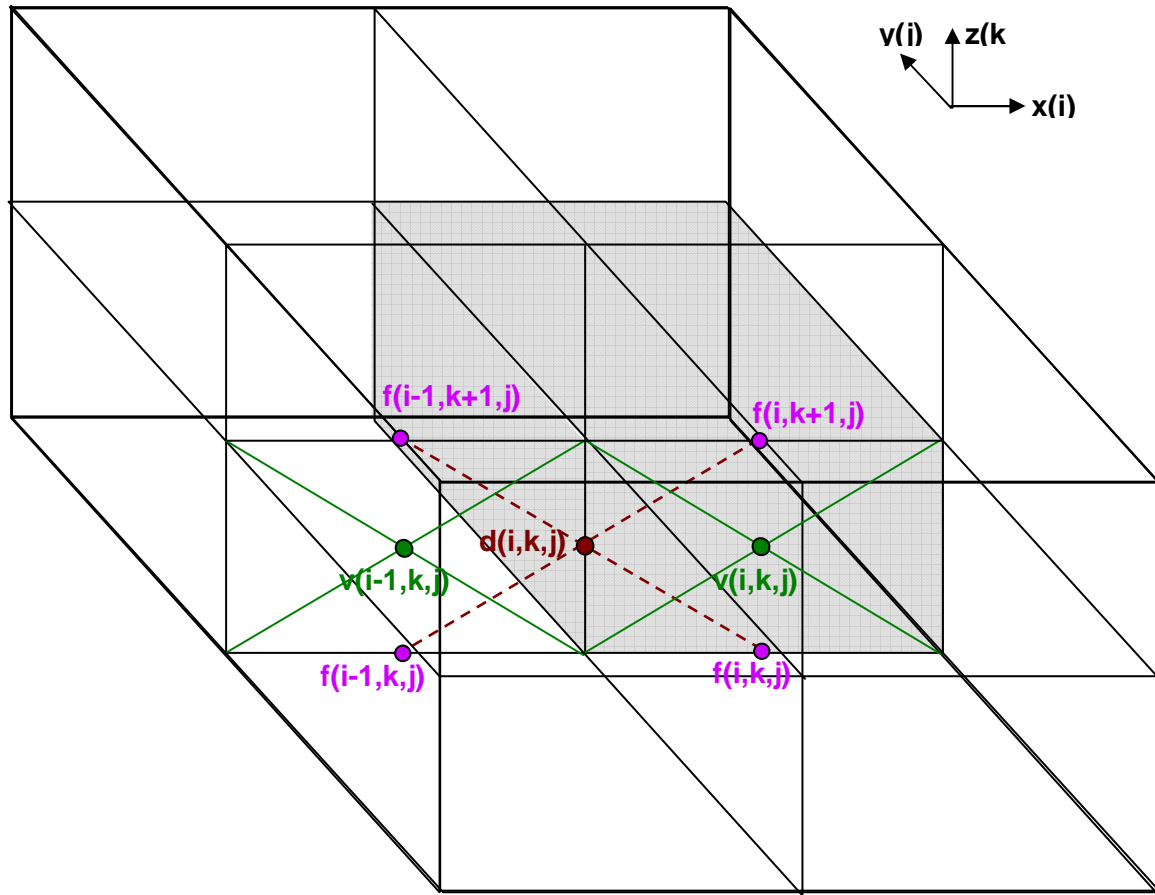
$${}^c \overline{c(i,k,j)}^d = 0.25 * (c(i-1,k,j) + c(i-1,k,j-1) + c(i,k,j-1) + c(i,k,j))$$



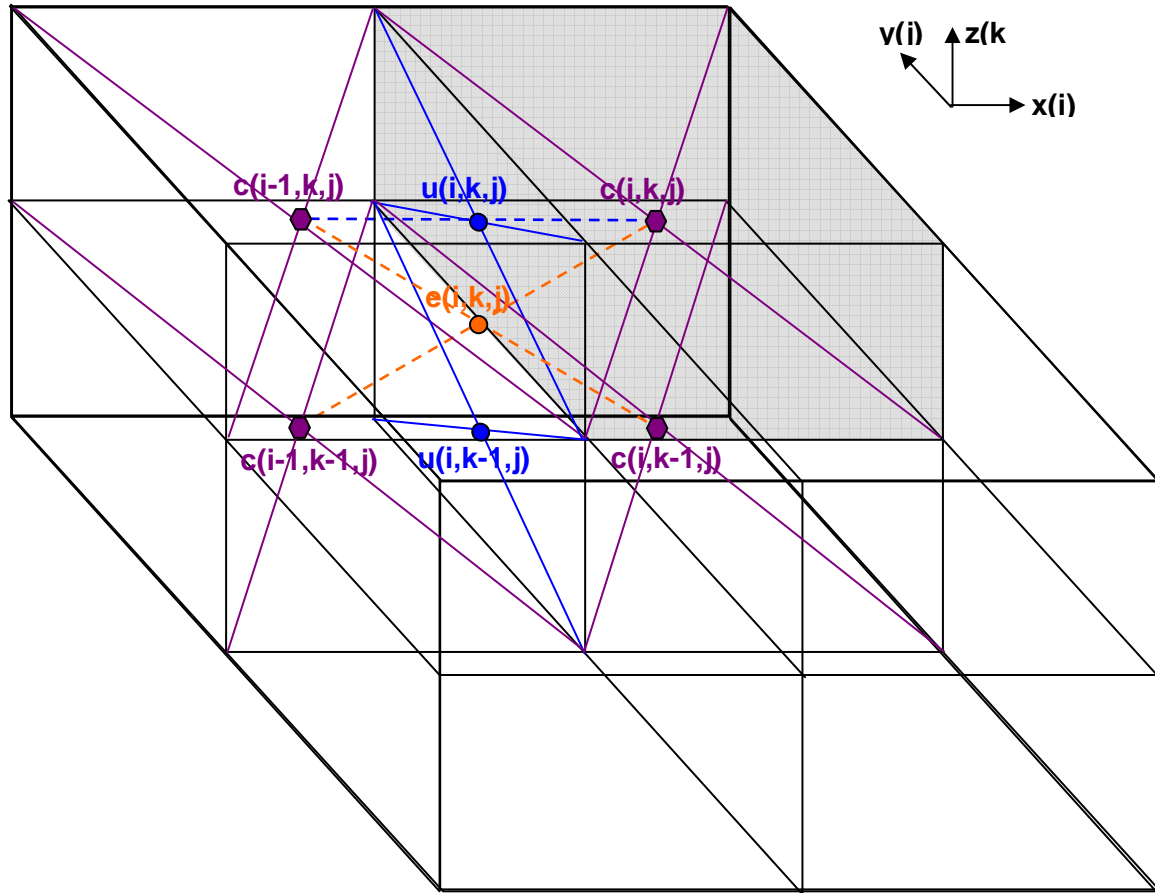
$${}^e \overline{e(i, k, j)}^d = 0.25 * (e(i, k, j) + e(i, k, j-1) + e(i, k+1, j-1) + e(i, k+1, j))$$



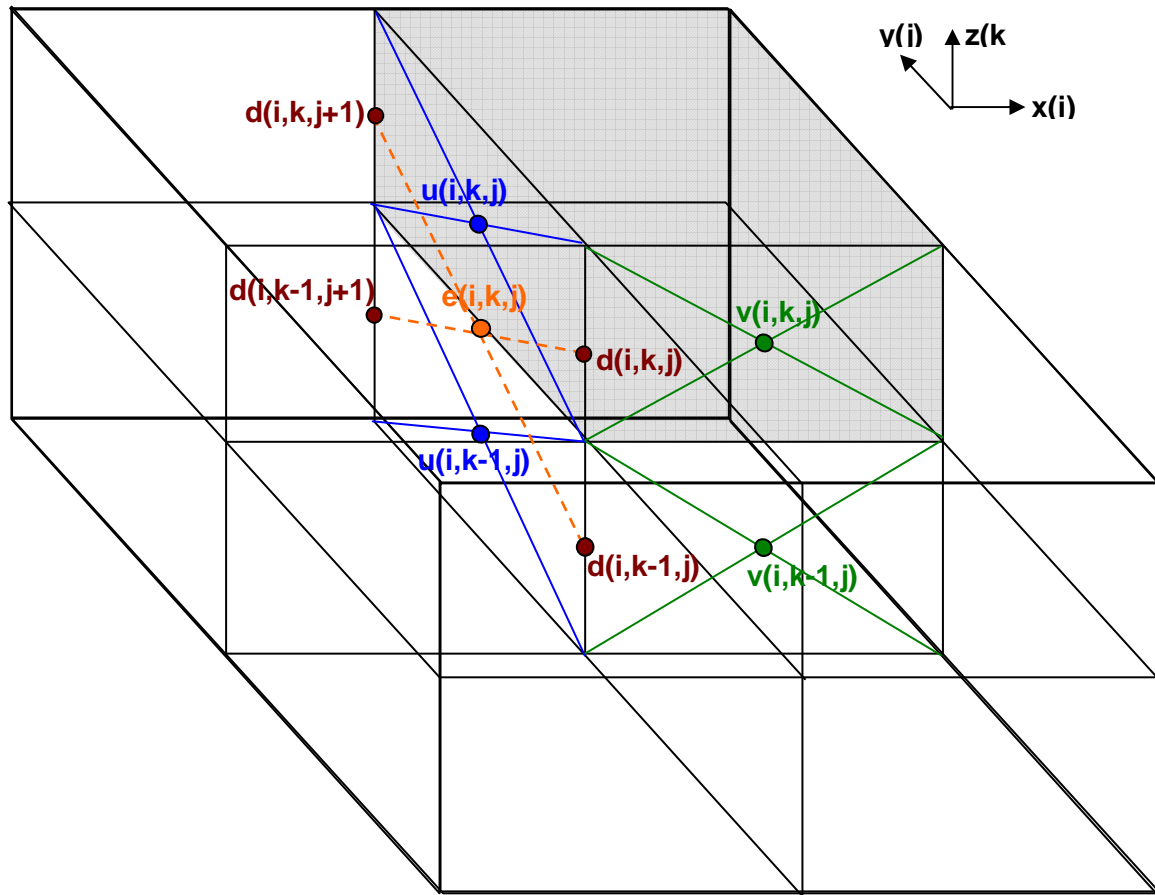
$$f \overline{f(i, k, j)}^d = 0.25 * (f(i-1, k, j) + f(i, k, j) + f(i, k+1, j) + f(i-1, k+1, j))$$



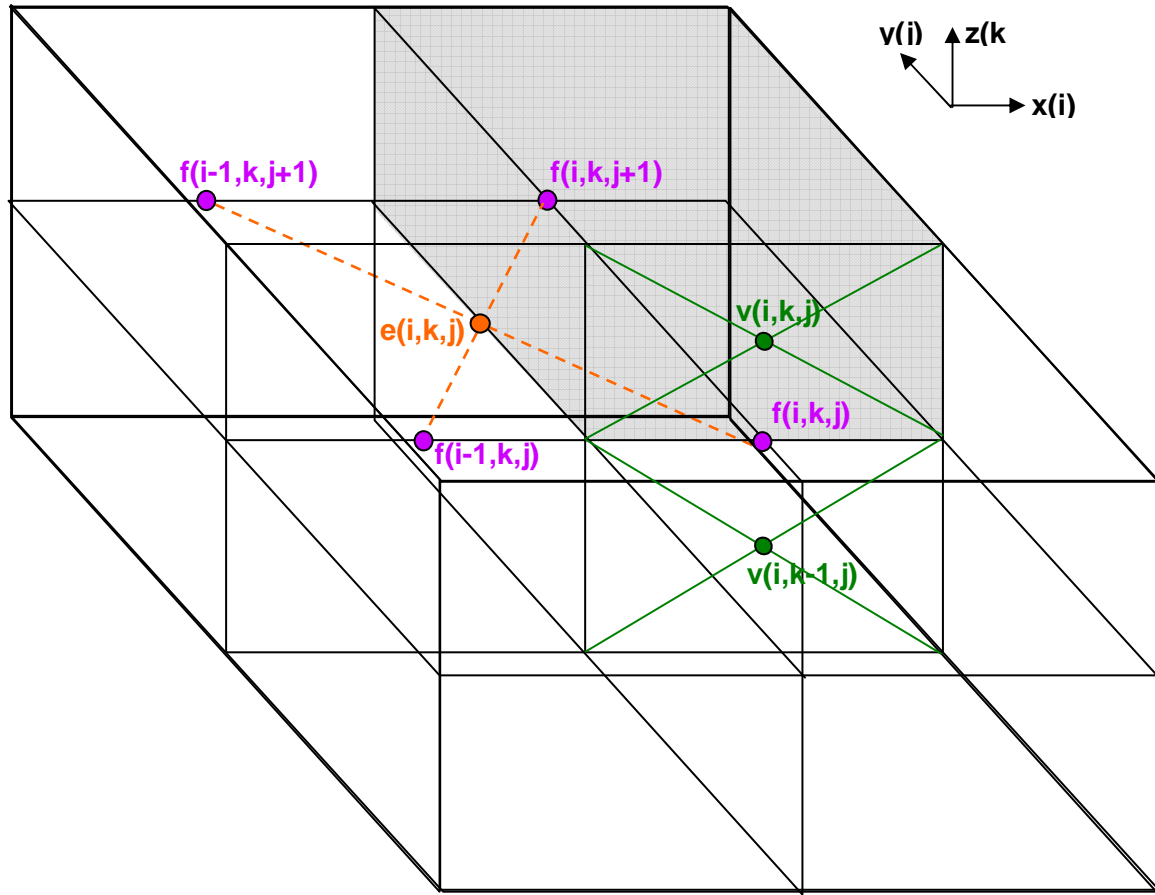
$${}^c \overline{c(i,k,j)}^e = 0.5 * (f_{nm}(k) * (c(i-1,k,j) + c(i,k,j)) + f_{np}(k) * (c(i,k-1,j) + c(i-1,k-1,j)))$$



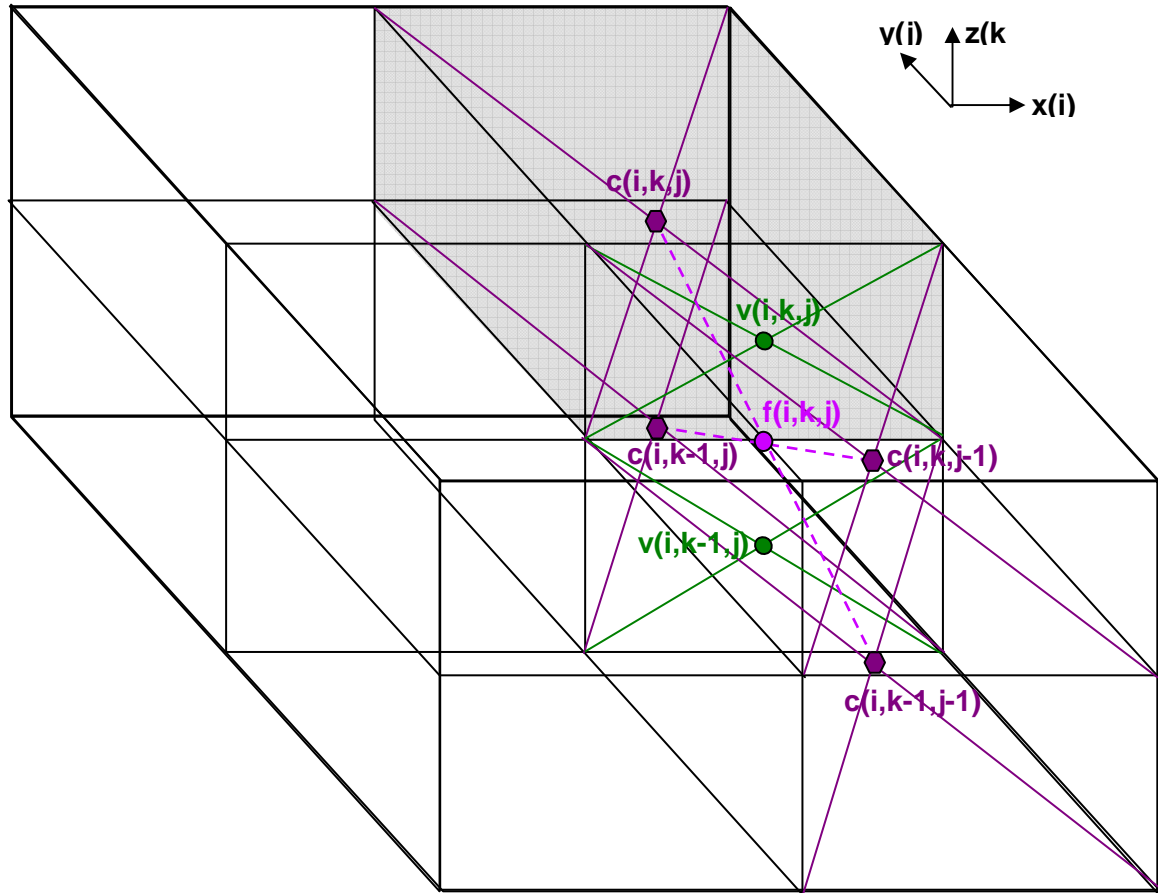
$$d \overline{d(i,k,j)}^e = 0.5 * (f_{nm}(k) * (d(i,k,j) + d(i,k,j+1)) + f_{np}(k) * (d(i,k-1,j) + d(i,k-1,j+1)))$$



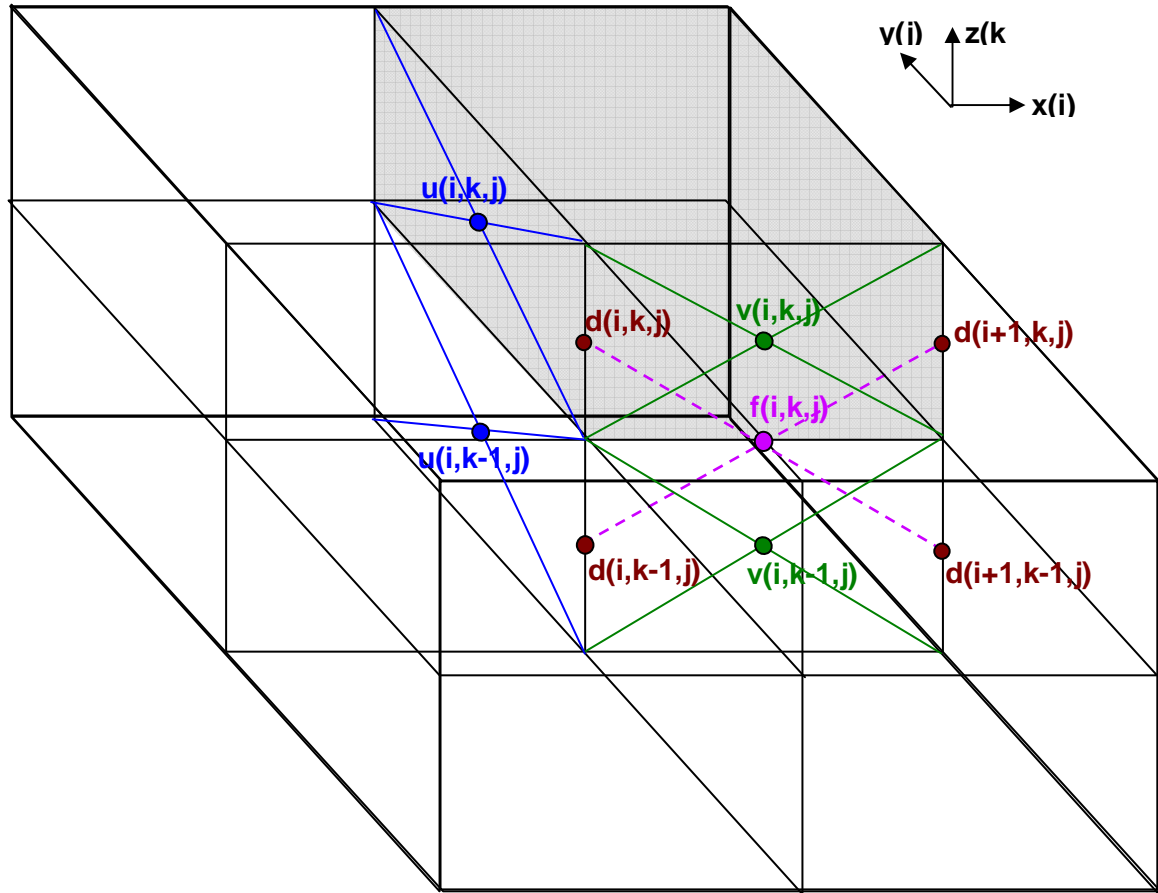
$$f \overline{f(i,k,j)}^e = 0.25 * (f(i-1,k,j+1) + f(i-1,k,j) + f(i,k,j) + f(i,k,j+1))$$



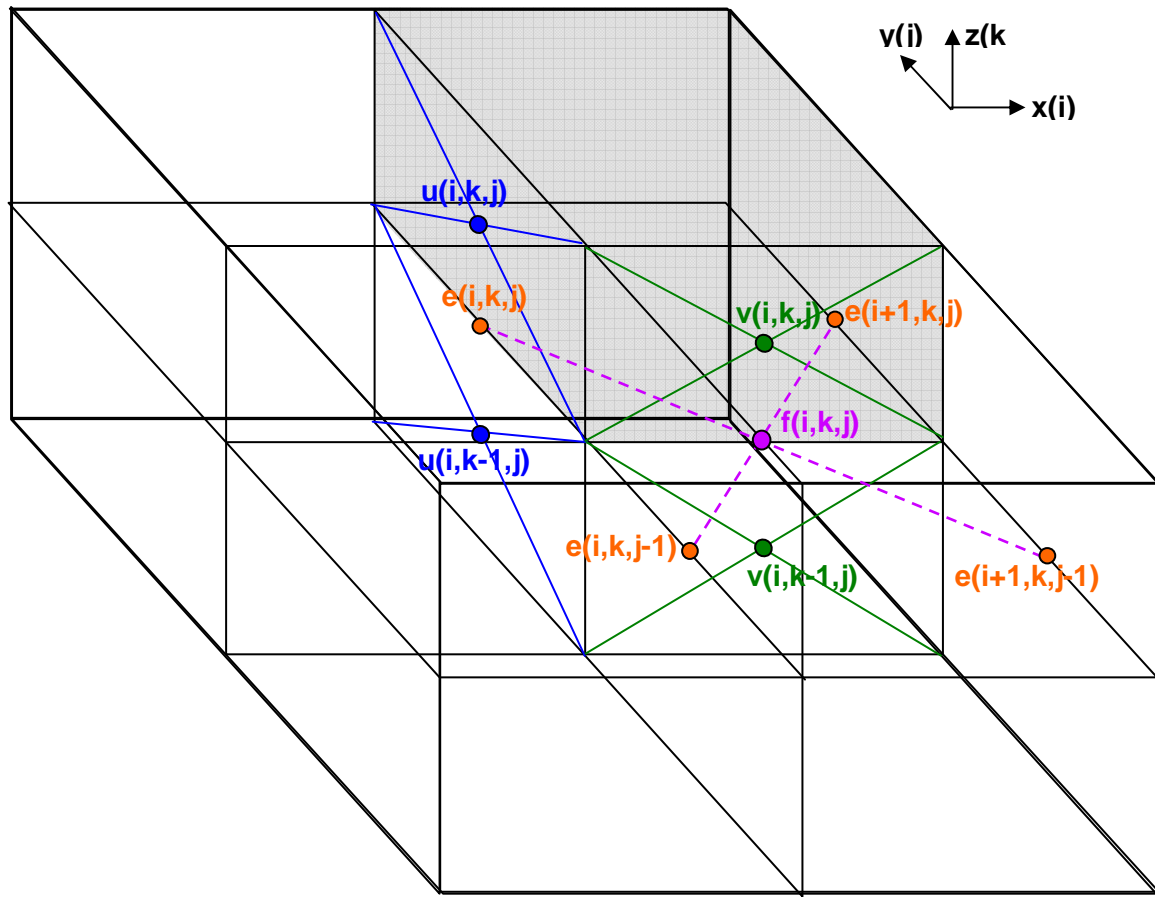
$${}^c \overline{c(i,k,j)}^f = 0.5 * (fnm(k) * (c(i,k,j) + c(i,k,j-1)) + fnp(k) * (c(i,k-1,j) + c(i,k-1,j-1)))$$



$$d \overline{d(i,k,j)}^f = 0.5 * (fnm(k) * (d(i,k,j) + d(i+1,k,j)) + fnp(k) * (d(i,k-1,j) + d(i+1,k-1,j)))$$



$${}^e \overline{e(i, k, j)}^f = 0.25 * (e(i, k, j) + e(i, k, j-1) + e(i+1, k, j-1) + e(i+1, k, j))$$

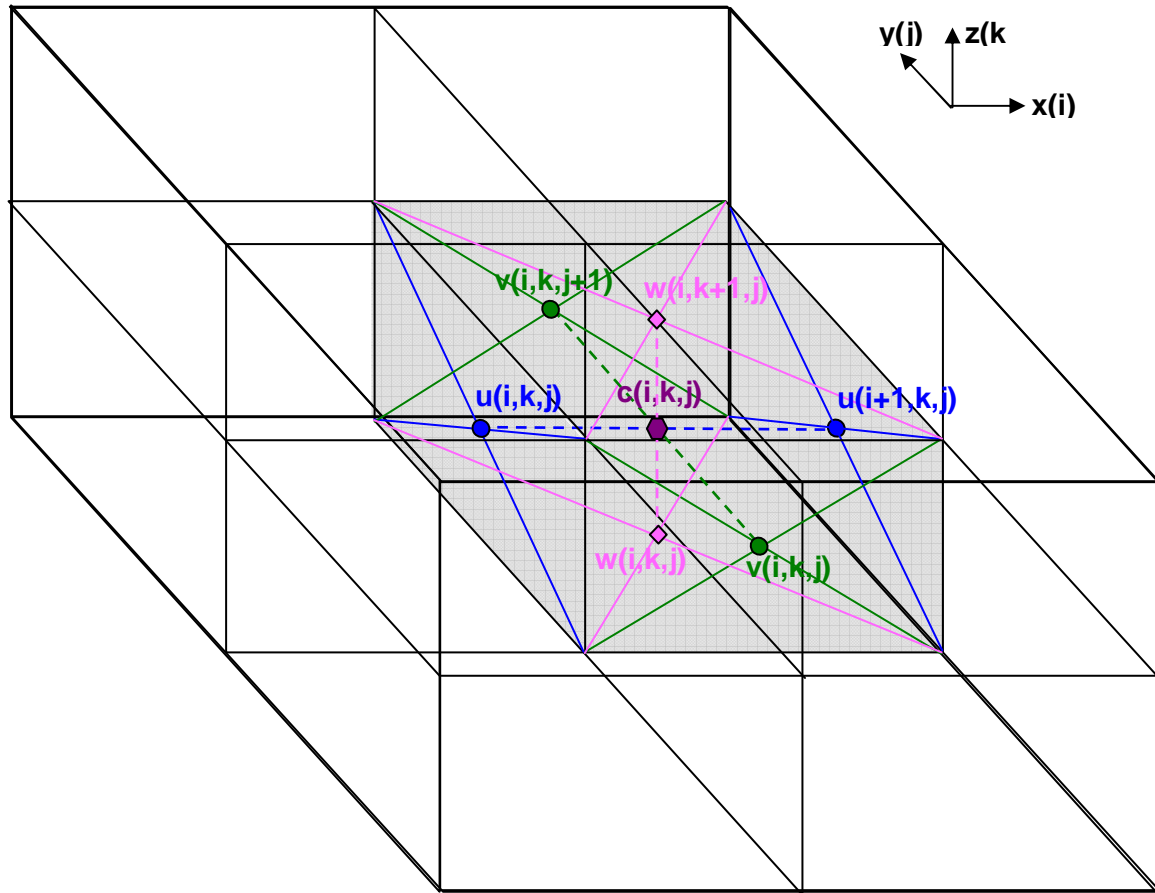


## Appendix D. Projections used by RSFS model

$${}^u \overline{u(i, k, j)}^c = 0.5 * (u(i, k, j) + u(i+1, k, j))$$

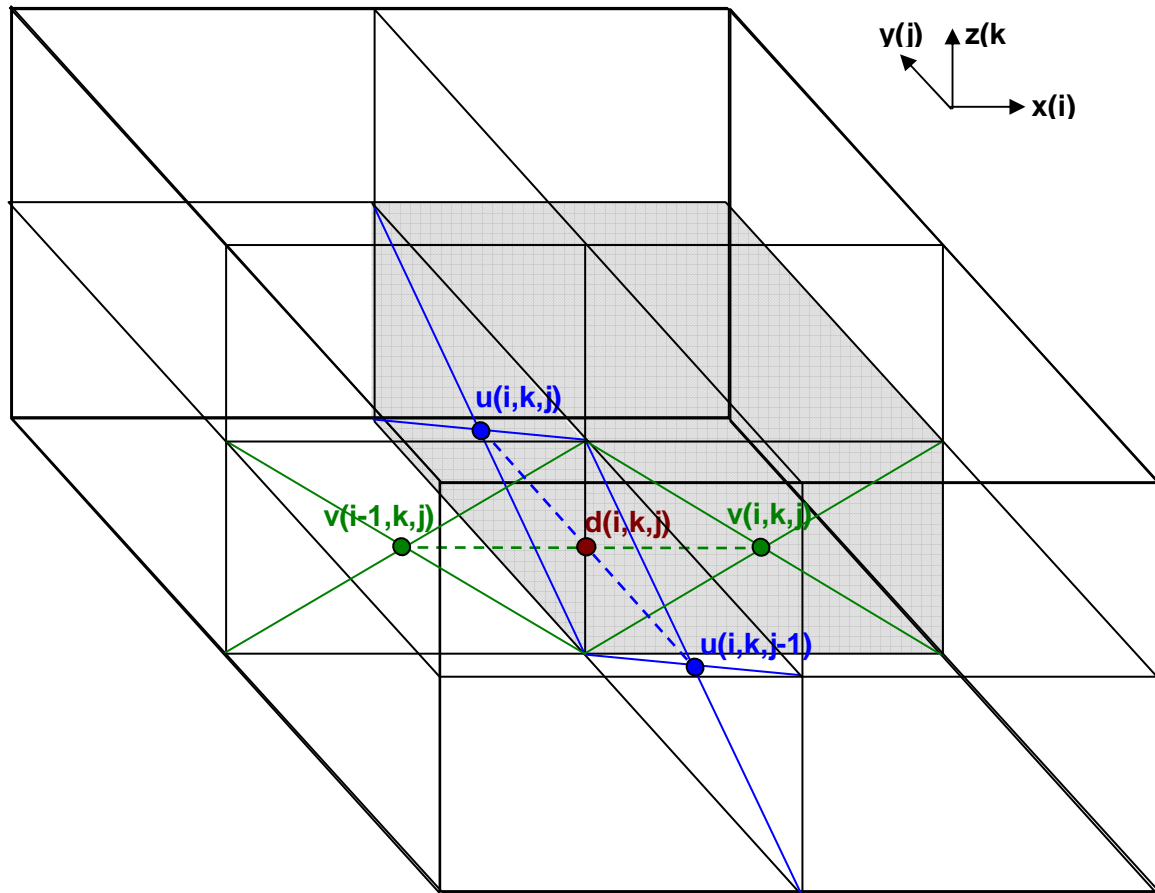
$${}^v \overline{v(i, k, j)}^c = 0.5 * (v(i, k, j) + v(i, k, j+1))$$

$${}^w \overline{w(i, k, j)}^c = 0.5 * (w(i, k, j) + w(i, k+1, j))$$



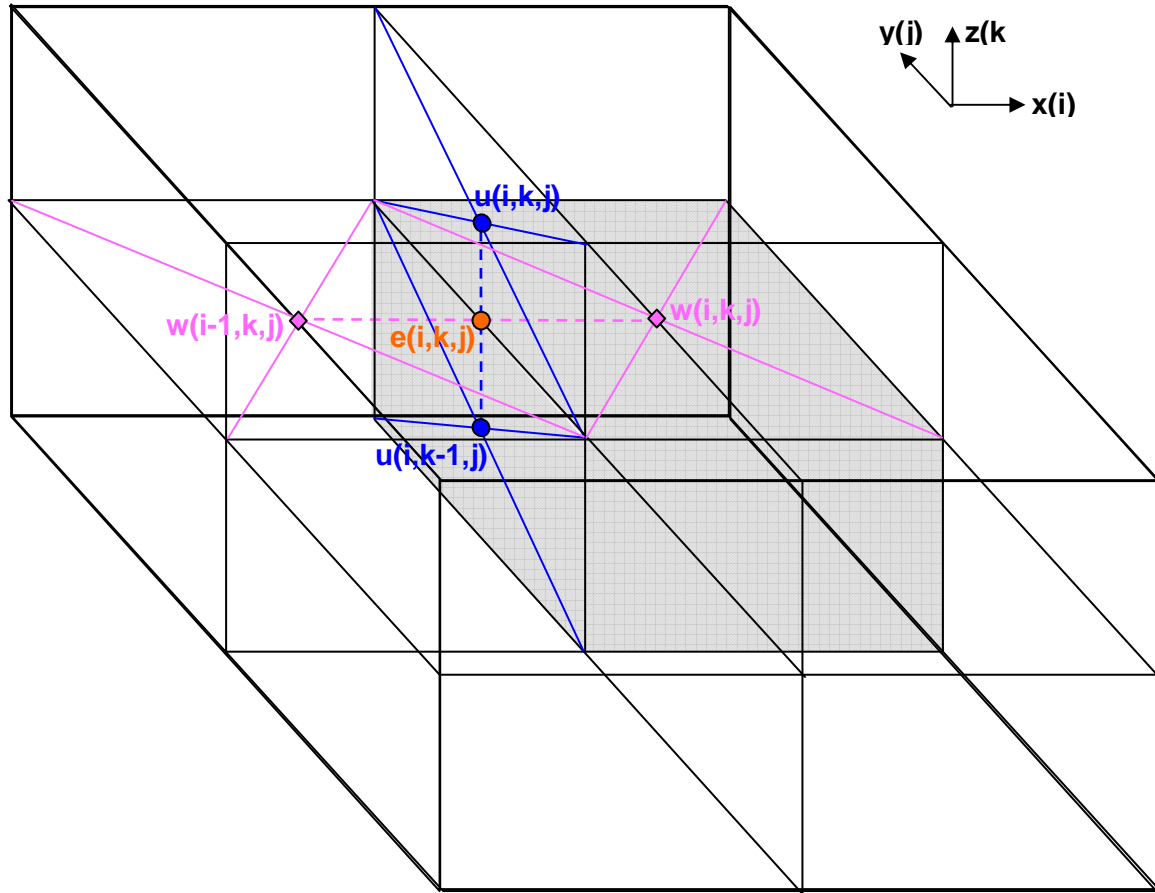
$${}^u \overline{u(i, k, j)}^d = 0.5 * (u(i, k, j) + u(i, k, j - 1))$$

$${}^v \overline{v(i, k, j)}^d = 0.5 * (v(i - 1, k, j) + v(i, k, j))$$



$$^u \overline{u(i, k, j)}^e = f_{nm} * u(i, k, j) + f_{np} * u(i, k - 1, j)$$

$$^w \overline{w(i, k, j)}^e = 0.5 * (w(i, k, j) + w(i - 1, k, j))$$



$${}^v \overline{v(i, k, j)}^e = f_{nm} * v(i, k, j) + f_{np} * v(i, k - 1, j)$$

$${}^w \overline{w(i, k, j)}^f = 0.5 * (w(i, k, j) + w(i, k, j - 1))$$

